






A Biosafety Level 2 Mouse Model for Studying Betacoronavirus-Induced Acute Lung Damage and Systemic Manifestations

Ana Cláudia dos Santos Pereira Andrade,^a Gabriel Henrique Campolina-Silva,^b Celso Martins Queiroz-Junior,^a Leonardo Camilo de Oliveira,^a Larisse de Souza Barbosa Lacerda,^a Jordane Clarisse Pimenta Gaggino,^a Filipe Resende Oliveira de Souza,^a Ian de Meira Chaves,^a Ingredy Beatriz Passos,^c Danielle Cunha Teixeira,^a Paloma Grazielle Bittencourt-Silva,^d Priscila Aparecida Costa Valadão,^a Leonardo Rossi-Oliveira,^a Maisa Mota Antunes,^a André Felipe Almeida Figueiredo,^a Natália Teixeira Wnuk,^a  Jairo R. Temerozo,^{e,f} André Costa Ferreira,^{g,h,i} Allysson Cramer,^b Cleida Aparecida Oliveira,^a  Ricardo Durães-Carvalho,^j Clarice Weis Arns,^j Pedro Pires Goulart Guimarães,^d Guilherme Mattos Jardim Costa,^a Gustavo Batista de Menezes,^a Cristina Guatimosim,^a Glauber Santos Ferreira da Silva,^d Thiago Moreno L. Souza,^{g,h} Breno Rocha Barrioni,^k Marivalda de Magalhães Pereira,^k Lirlândia Pires de Sousa,^l Mauro Martins Teixeira,^b  Vivian Vasconcelos Costa^{a,b}

^aDepartment of Morphology, Institute of Biological Sciences, Universidade Federal de Minas Gerais, Belo Horizonte, MG, Brazil

^bDepartment of Biochemistry and Immunology, Institute of Biological Sciences, Universidade Federal de Minas Gerais, Belo Horizonte, MG, Brazil

^cDepartment of Microbiology, Institute of Biological Sciences, Universidade Federal de Minas Gerais, Belo Horizonte, MG, Brazil

^dDepartment of Physiology and Biophysics, Institute of Biological Sciences, Universidade Federal de Minas Gerais, Belo Horizonte, MG, Brazil

^eLaboratory on Thymus Research, Oswaldo Cruz Institute, Fiocruz, Rio de Janeiro, RJ, Brazil

^fNational Institute for Science and Technology on Neuroimmunomodulation, Oswaldo Cruz Foundation (Fiocruz), Rio de Janeiro, RJ, Brazil

^gNational Institute for Science and Technology on Innovation on Diseases of Neglected Populations (INCT/IDNP), Center for Technological Development in Health (CDTS), Oswaldo Cruz Foundation (Fiocruz), Rio de Janeiro, RJ, Brazil

^hImmunopharmacology Laboratory, Oswaldo Cruz Foundation (Fiocruz), Rio de Janeiro, RJ, Brazil

ⁱLaboratório de Pesquisas Pré-clínicas, Universidade Iguazu (UNIG), Rio de Janeiro, RJ, Brazil

^jLaboratory of Virology, Universidade Estadual de Campinas (UNICAMP), Campinas, SP, Brazil

^kDepartment of Metallurgical Engineering and Materials, Federal University of Minas Gerais, School of Engineering, Belo Horizonte, Brazil

^lDepartment of Clinical and Toxicological Analysis, Faculty of Pharmacy, Universidade Federal de Minas Gerais, Belo Horizonte, MG, Brazil

Ana Cláudia dos Santos Pereira Andrade and Gabriel Henrique Campolina-Silva contributed equally to this work. Co-first authorship order was determined based on who initiated the study.

ABSTRACT The emergence of life-threatening zoonotic diseases caused by betacoronaviruses, including the ongoing coronavirus disease 19 (COVID-19) pandemic, has highlighted the need for developing preclinical models mirroring respiratory and systemic pathophysiological manifestations seen in infected humans. Here, we showed that C57BL/6J wild-type mice intranasally inoculated with the murine betacoronavirus murine hepatitis coronavirus 3 (MHV-3) develop a robust inflammatory response leading to acute lung injuries, including alveolar edema, hemorrhage, and fibrin thrombi. Although such histopathological changes seemed to resolve as the infection advanced, they efficiently impaired respiratory function, as the infected mice displayed restricted lung distention and increased respiratory frequency and ventilation. Following respiratory manifestation, the MHV-3 infection became systemic, and a high virus burden could be detected in multiple organs along with morphological changes. The systemic manifestation of MHV-3 infection was also marked by a sharp drop in the number of circulating platelets and lymphocytes, besides the augmented concentration of the proinflammatory cytokines interleukin 1 beta (IL-1 β), IL-6, IL-12, gamma interferon (IFN- γ), and tumor necrosis factor (TNF), thereby mirroring some clinical features observed in moderate and severe cases of COVID-19. Importantly, both respiratory and systemic changes triggered by MHV-3 infection were greatly prevented by blocking TNF signaling, either via genetic or pharmacologic approaches. In line with this, TNF blockage also diminished the infection-mediated release of proinflammatory cytokines and virus replication of human

Citation Andrade ACDS, Campolina-Silva GH, Queiroz-Junior CM, de Oliveira LC, Lacerda LDSB, Gaggino JCP, de Souza FRO, de Meira Chaves I, Passos IB, Teixeira DC, Bittencourt-Silva PG, Valadão PAC, Rossi-Oliveira L, Antunes MM, Figueiredo AFA, Wnuk NT, Temerozo JR, Ferreira AC, Cramer A, Oliveira CA, Durães-Carvalho R, Weis Arns C, Guimarães PPG, Costa GMJ, de Menezes GB, Guatimosim C, da Silva GSF, Souza TML, Barrioni BR, Pereira MDM, de Sousa LP, Teixeira MM, Costa VV. 2021. A biosafety level 2 mouse model for studying betacoronavirus-induced acute lung damage and systemic manifestations. *J Virol* 95:e01276-21. <https://doi.org/10.1128/JVI.01276-21>.

Editor Stacey Schultz-Cherry, St. Jude Children's Research Hospital

Copyright © 2021 American Society for Microbiology. All Rights Reserved.

Address correspondence to Vivian Vasconcelos Costa, vivianvcosta@ufmg.br.

Received 29 July 2021

Accepted 1 September 2021

Accepted manuscript posted online 8 September 2021

Published 27 October 2021

epithelial lung cells infected with severe acute respiratory syndrome coronavirus 2 (SARS-CoV-2). Collectively, results show that MHV-3 respiratory infection leads to a large range of clinical manifestations in mice and may constitute an attractive, lower-cost, bio-safety level 2 (BSL2) *in vivo* platform for evaluating the respiratory and multiorgan involvement of betacoronavirus infections.

IMPORTANCE Mouse models have long been used as valuable *in vivo* platforms to investigate the pathogenesis of viral infections and effective countermeasures. The natural resistance of mice to the novel betacoronavirus SARS-CoV-2, the causative agent of COVID-19, has launched a race toward the characterization of SARS-CoV-2 infection in other animals (e.g., hamsters, cats, ferrets, bats, and monkeys), as well as adaptation of the mouse model, by modifying either the host or the virus. In the present study, we utilized a natural pathogen of mice, MHV, as a prototype to model betacoronavirus-induced acute lung injury and multiorgan involvement under biosafety level 2 conditions. We showed that C57BL/6J mice intranasally inoculated with MHV-3 develops severe disease, which includes acute lung damage and respiratory distress that precede systemic inflammation and death. Accordingly, the proposed animal model may provide a useful tool for studies regarding betacoronavirus respiratory infection and related diseases.

KEYWORDS betacoronavirus, MHV-3, lung infection, COVID-19, animal model, tumor necrosis factor

The *Betacoronavirus* genus belongs to the *Coronaviridae* family and encompasses positive-stranded enveloped RNA viruses. This viral group is broadly distributed among humans and other mammals, including rodents, bats, pigs, and ruminants (1–3). The high prevalence of betacoronaviruses all over the world, combined with their great genetic diversity and the increased human occupation of isolated ecosystems, makes the periodic emergence of novel coronaviruses in zoonotic outbreaks highly probable after host escape events (1). In fact, over the last 2 decades, there were three isolated zoonotic outbreaks of severe coronavirus infection in humans, including the currently circulating severe acute respiratory syndrome coronavirus 2 (SARS-CoV-2), which is responsible for the ongoing coronavirus disease 2019 (COVID-19) pandemic (4). Due to their epidemiological importance, a deeper understanding of viral biology, pathogenesis, and the discovery of therapeutic options against betacoronaviruses is imperative.

COVID-19 has a broad spectrum of clinical manifestations. While in most cases, SARS-CoV-2 respiratory infection is silent or triggers only mild respiratory symptoms, in others it leads to severe conditions, including acute respiratory distress syndrome (ARDS), systemic inflammation, multiorgan failure, and death (5, 6). Several animal models have been proposed as preclinical platforms to study the pathogenesis of SARS-CoV-2, including mice, ferrets, Syrian hamsters, and primates. (7–12). The inherent resistance of wild-type mice to SARS-CoV-2 infection led to the establishment of strategies to adapt these rodents to infection by modifying either the host or the virus (9, 13, 14). One of the most common strategies has been the infection of transgenic mice expressing human ACE2 (hACE2) using SARS-CoV-2 strains. However, these animal models in general fail to reproduce the prolonged pneumonia with severe manifestations and multiorgan impairment, besides displaying a high rate of SARS-CoV-2 replication in nontarget tissues (15, 16). Due to interspecies differences, a set of diverse models is necessary for a broader understanding of viral tropism, replication, dissemination, clinical signs, pathogenesis, and immune response caused by SARS-CoV-2 (17).

The use of other betacoronaviruses, such as the murine coronavirus, has been suggested as a strategy to emulate many of the key aspects of human coronavirus infection (18, 19). Among murine coronaviruses, the group known as murine hepatitis coronavirus (MHV) is the prototype of this genus and a natural pathogen of the *Mus musculus* species (20). MHV is capable of inducing a severe and lethal disease in mice,

and some of its variants, such as MHV-1 and MHV-A59, may have an initial pulmonary tropism when inoculated intranasally, before systemic dissemination. Thus, targeting MHV respiratory infection may constitute a promising preclinical platform to mirror betacoronavirus-induced pathophysiological features seen in humans, including severe acute respiratory syndrome (18, 19, 21). An important advantage of using this murine model is the requirement for biosafety level 2 (BSL2), which makes this model significantly less costly and safer for screening compounds of therapeutic interest.

The murine hepatitis virus strain 3 (MHV-3) has classically been described as a causative agent of severe hepatitis in several strains of mice (20). Due to its hepatotropism, the potential of this MHV strain to also cause respiratory disease during an intranasal infection has been poorly investigated. In this work, we showed that intranasal infection of wild-type mice with MHV-3 produced a transient respiratory disease with pulmonary functional impairment before leading to systemic inflammation, multiorgan injury, and death. We also showed that the MHV-3-induced pulmonary and extrapulmonary manifestations were dependent on tumor necrosis factor (TNF) signaling.

RESULTS

Intranasally delivered MHV-3 favors pulmonary viral replication in C57BL/6J mice. To characterize a mouse model of coronavirus-induced acute respiratory infection inside a BSL2 facility, 6- to 7-week-old C57BL/6J mice were inoculated via the intranasal route with 10^3 PFU of MHV-3 and monitored daily for signs of illness (Fig. 1a). Following infection, mice underwent significant weight loss, which started on the third day postinfection (dpi), and they became moribund and died by 6 dpi (Fig. 1b and c). Male and female animals succumbed similarly to the disease, as their median survival times upon MHV-3 challenge were 5.5 and 6 days, respectively. MHV-3 infection was also lethal at a lower dose (10^2 PFU); however, there was a modest delay in weight loss and death compared to that observed at a higher inoculum (Fig. 1b and c).

Intranasal infection of mice with 10^3 PFU led to progressive thrombocytopenia (Fig. 1d). The number of circulating leukocytes also decreased as the infection progressed and was mostly driven by the sharp lymphopenia observed from 3 dpi onwards (Fig. 1d and e). Thermal response to viral infection was also observed. As depicted in Fig. 1f, body temperature began to rise slowly 24 h after virus inoculation. At 2 and 3 dpi, mice reached $37.4^\circ\text{C} \pm 0.3^\circ\text{C}$ and $38.1^\circ\text{C} \pm 0.2^\circ\text{C}$, respectively, both of which were significantly higher than the average temperature recorded over 3 days before infection ($36.3^\circ\text{C} \pm 0.1^\circ\text{C}$; $P < 0.05$) (Fig. 1f and g). It is worth noting that major changes in body temperature occurred during the light phase, which is the resting period for nocturnal habit animals (Fig. 1g).

To ascertain whether intranasal delivered MHV-3 favors viral replication in the respiratory system, viral load was assessed in the lung at 1, 3, and 5 dpi and compared with that found in the plasma, liver, spleen, heart, kidney, brain, and testes. Results confirmed the lungs as the initial replication site of MHV-3, as assessed by the presence of infectious virus in this tissue, with viral loads significantly increasing from 1 dpi to 5 dpi (Fig. 1h). Conversely, viruses were recovered from 3 dpi onwards in other organs, with viremia being more stably detected at 5 dpi (Fig. 1h and i). Together, these data show that C57BL/6J mice are highly susceptible to intranasal inoculation of MHV-3 and that lungs are likely the primary site of viral infection and replication.

MHV-3 triggers inflammation-associated lung damage and respiratory dysfunction. We next investigated whether MHV-3 infection would affect lung morphology and trigger inflammation-associated tissue damage (Fig. 2a). Compared to mock controls, a higher number of cells stained for the panleukocyte marker CD45 was found in the lung sections of infected mice after 1 day and especially 3 days after inoculation (Fig. 3b). Flow cytometry results concurred with the recruitment of leukocytes to the lung tissue early during infection, showing a significant rise in the percentage of neutrophils and macrophages/monocytes. On the other hand, we found that the percentage of both CD4^+ and CD8^+ T cells in the lung gradually decreased as the infection progressed (Fig. 2c). The histopathologic examination of lung sections revealed that

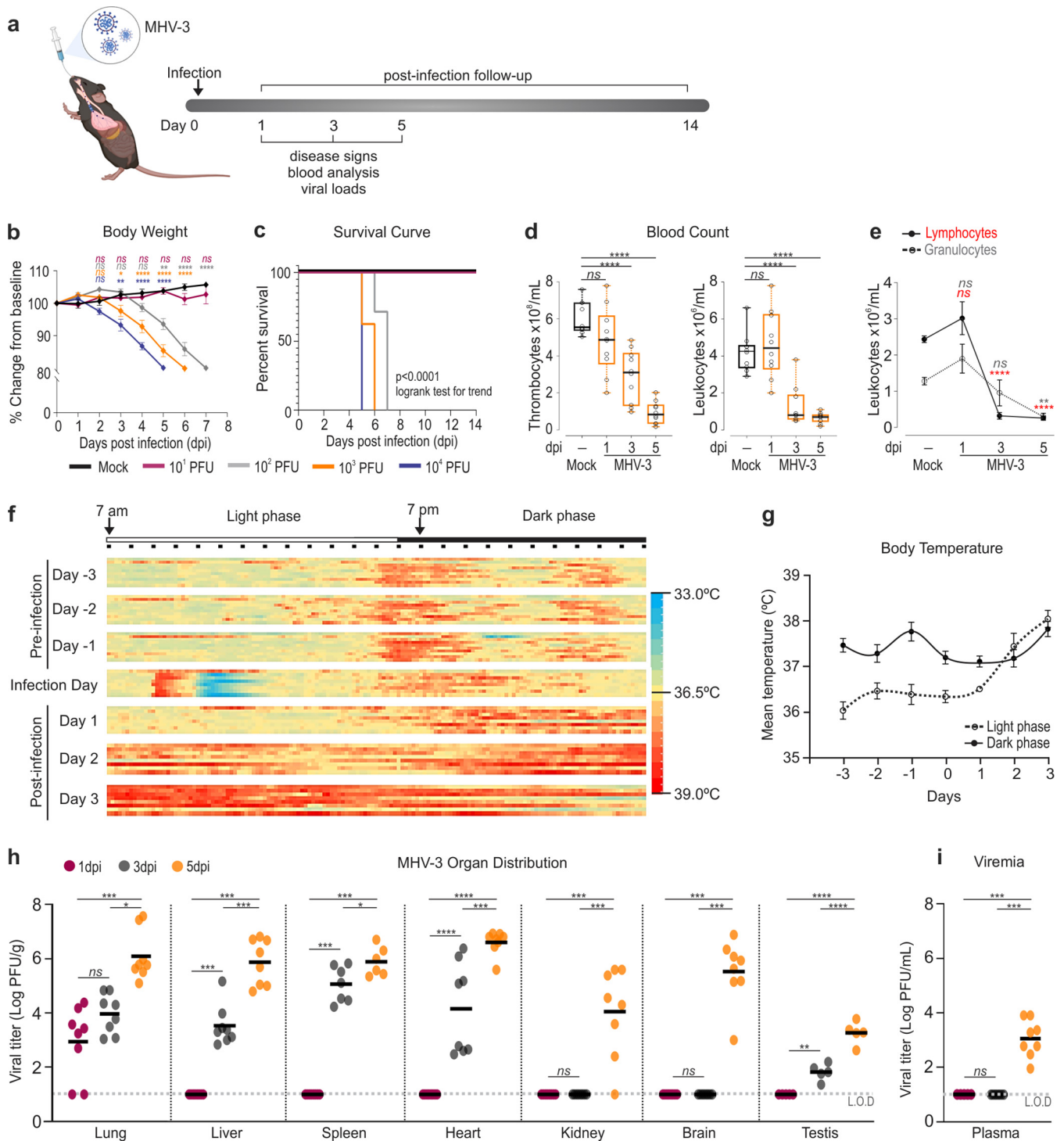


FIG 1 Intrasally inoculated MHV-3 triggers lethal disease in C57BL/6J mice. (a) Experimental design. (b) Body weight change upon infection assessed by two-way repeated-measures analysis of variance (ANOVA) plus Sidak's multiple-comparison test (mean ± standard error of the mean [SEM]; *n* = 8). (c) Kaplan-Meier survival curve of infected mice versus mock controls (*n* = 8). (d) Changes in the number of circulating thrombocytes and leukocytes over 5 days postinoculation (dpi), represented as box plots. The whiskers go from the first and third quartiles to the minimum or maximum value. Data from each infection time were compared with those from the mock group by one-way ANOVA plus Dunnett's multiple-comparison test (*n* = 10). (e) Differential blood count highlighting the sharp infection-related drop of lymphocyte counts that likely guided leukopenia noticed from 3 dpi onwards. Differences between infection groups and the mock control were assessed by one-way ANOVA plus Dunnett's multiple-comparison test (mean ± SEM; *n* = 6). (f) Heatmap showing the body temperatures recorded in a group of 10 mice over 3 days pre- and postinfection. Note an increase in the mean temperature on 2 and 3 dpi, especially in the light phase. (g) Means ± SEM of body temperatures depicted in panel f according to the time of the day. (h, i) Viral load determined in organ extracts and plasma of MHV-3-infected mice by plaque assay. The results are presented as log₁₀ PFU per gram of tissue or milliliter of plasma. Differences among groups were assessed by Kruskal-Wallis plus Dunn's *post hoc* test (*n* = 5 to 8). LOD, limit of detection. ns, not significant (*P* > 0.05); *, *P* < 0.05; **, *P* < 0.01; ***, *P* < 0.001; ****, *P* < 0.0001.

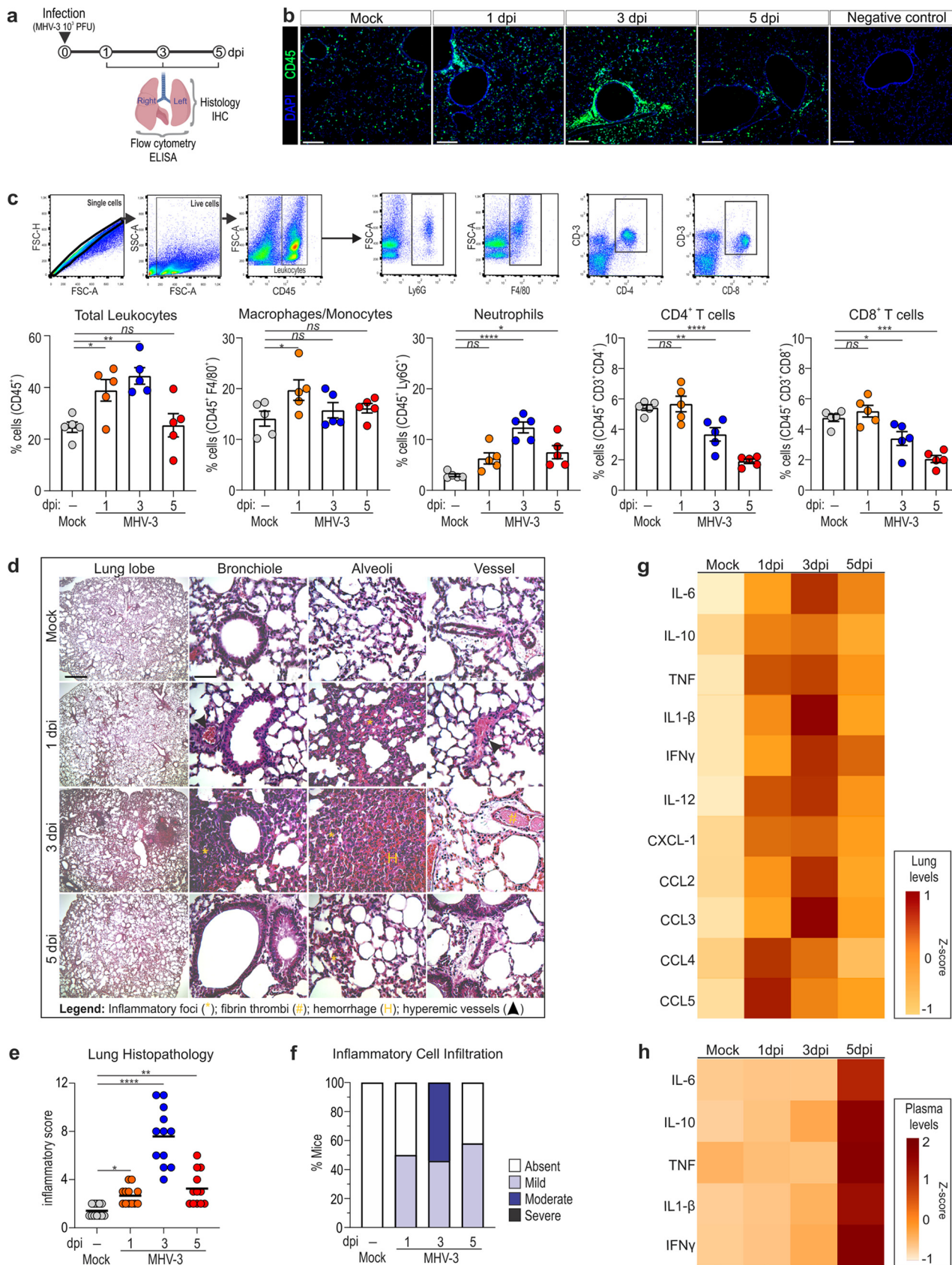


FIG 2 MHV-3 infection triggers inflammation-associated lung injury. (a) Experimental design. (b) Representative confocal three-dimensional (3D) image showing high abundance of CD45⁺ leukocytes (green staining) in the lungs of mice at 1 and 3 dpi. (c) Flow cytometry analyses showing the (Continued on next page)

MHV-3 infection triggered transient inflammation-associated lung injury. As such, approximately 50% of mice had discrete inflammatory cell infiltration in close association with areas of alveolar edema and hyperemic vessels at 1 day after MHV-3 infection (Fig. 2d to f). At 3 dpi, the inflammatory infiltrate became robust and widespread throughout the lung tissue, leading to greater histopathological changes. Inflammation foci were frequently seen in the vicinity of bronchioles, in perivascular areas, and in the lumen of hyperemic vessels (Fig. 2b, d, e, and f). Some blood vessels presented eosinophilic fibrillar material adherent to the vascular wall, which is characteristic of fibrin thrombi. In some samples, areas of necrosis and hemorrhage were also observed (Fig. 2d). Conversely, the inflammation-associated lung damage in the mouse lung at 5 dpi was milder and encompassed the changes portrayed here for day 1 after infection (Fig. 2d to f), suggesting that inflammation was resolving.

The intrapulmonary concentration of major chemokines (CCL2, CCL3, CCL4, and CCL5) and cytokines (TNF, interleukin 6 [IL-6], IL-1 β , IL-12, and gamma interferon [IFN- γ]) was markedly increased at 1 dpi and/or 3 dpi and decreased thereafter (Fig. 2g). In contrast, high levels of the inflammatory mediators (IL-6, IL-10, TNF, IL-1 β , and IFN- γ) were only detected in the blood at 5 dpi (Fig. 2h). These data suggest that the current infection model exhibits transient pulmonary pneumonia followed by systemic inflammation.

Next, we asked whether these histopathological changes could impact lung function. By using the whole-body plethysmography method, two control preinfection measurements of ventilatory parameters were performed in freely moving mice and compared with that recorded on 3 dpi (Fig. 3a). Interestingly, there was an increase in respiratory frequency in MHV-3-infected animals (Fig. 3b) that was characterized by shortened respiratory cycles (expiration/inhalation event; see Fig. 3b). In addition, the mechanics of the respiratory system were evaluated invasively in another group of mice at 3 dpi and compared to those of mock controls (Fig. 3a). There was restricted lung distention after MHV-3 infection, as determined by the lower static compliance of the respiratory system (Fig. 3c). There was also a decrease in vital capacity of the infected group (Fig. 3c). These restrictive aspects of pulmonary function are likely secondary to the pulmonary inflammation and damage. These data suggest that intranasal inoculation of MHV-3 in C57BL/6J mice triggers dysfunction of the respiratory system.

Given the pivotal role of diaphragm contraction for breathing and the recent evidence that SARS-CoV-2 might trigger diaphragm myopathy (22), we next checked the integrity of diaphragm neuromuscular junctions (NMJs) in the current infection model. By combining whole-mount confocal microscopy and computer-assisted image analysis, we showed that NMJs from MHV-3-infected mice at 3 and 5 dpi were significantly smaller and more fragmented at both pre- and postsynaptic endings compared to those of mock controls (Fig. 4). Although this deterioration of the diaphragm synaptic apparatus may not be sufficient to disrupt pulmonary ventilation in infected mice, we do not rule out the possibility that coronavirus-induced denervation at diaphragm NMJs could account for respiratory failure in the long term, which could be of particular interest for COVID-19 patients under mechanical ventilatory support.

MHV-3 induces extrapulmonary damage. MHV-3 is a murine coronavirus well-known for its hepatotropism (20). Overall, intranasally inoculated MHV-3 triggered hepatitis and liver necrosis, especially at 5 dpi (Fig. 5), the period that preceded systemic

FIG 2 Legend (Continued)

percentages among groups of total leukocytes, macrophages/monocytes, neutrophils, and CD4⁺ and CD8⁺ T cells. The percentage of each cell type at 1, 3, and 5 dpi was estimated following the representative gating scheme (upper panels) and compared with that found in the mock group by one-way ANOVA plus Dunnett's multiple-comparison test (mean \pm SEM; $n = 5$). (d) Hematoxylin and eosin (H&E) staining of lung sections showing notorious signs of inflammatory injury in infected mice. Bars, 450 μ m (low magnification) and 50 μ m (high magnification). (e) Histopathological assessment in relation to overall inflammatory score. Comparisons between mock and infection groups were carried out by Kruskal-Wallis plus Dunn's *post hoc* test ($n = 12$). (f) Percentages of mice according to the grade of inflammatory cell infiltration. (g) Heatmap evidencing changes in the levels of cytokines and chemokines measured by enzyme-limited immunosorbent assay (ELISA) in the lung of mock controls and MHV-3-infected mice ($n = 5$). (h) Heatmap showing greatly higher levels of IL-6, IL-10, TNF, IL-1 β , and IFN- γ in the plasma of infected mice at 5 dpi ($n = 5$). ns, not significant ($P > 0.05$); *, $P < 0.05$; **, $P < 0.01$; ***, $P < 0.001$; ****, $P < 0.0001$.

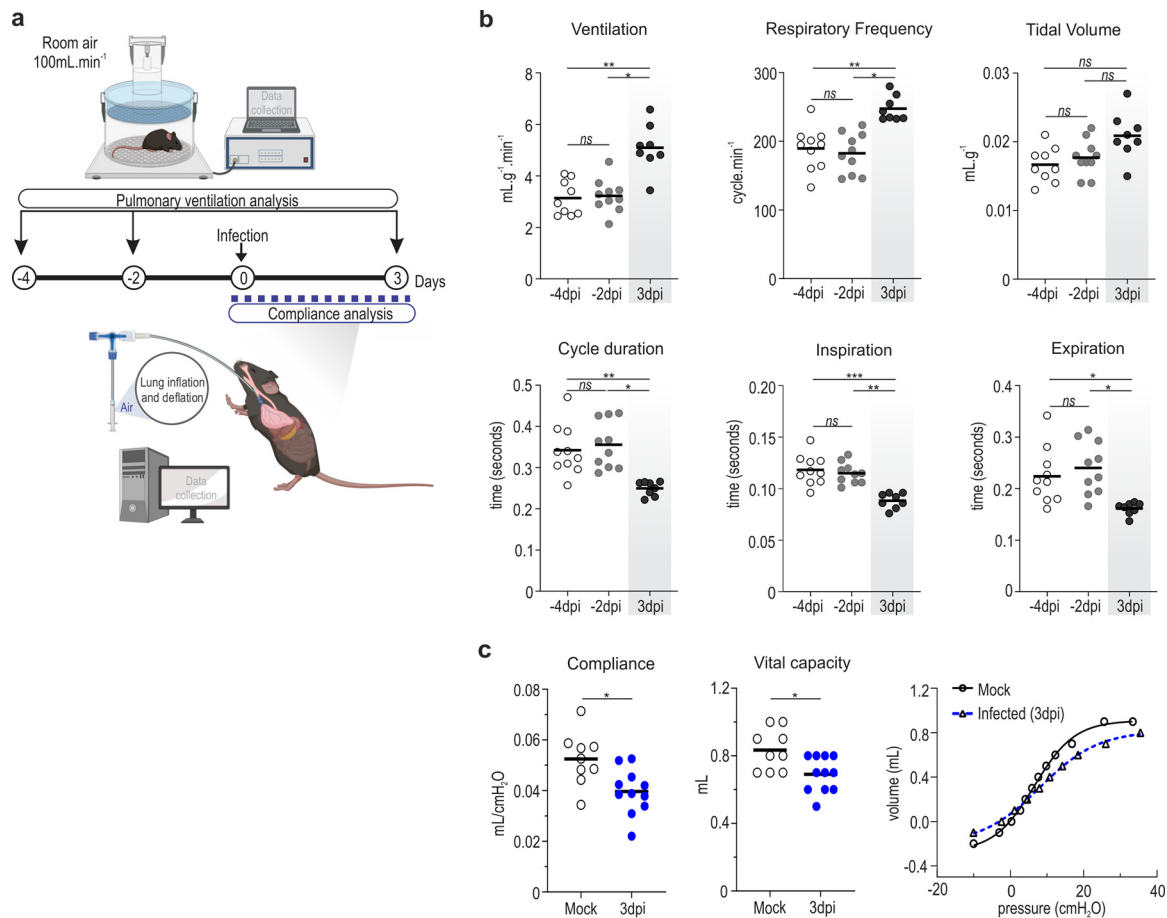


FIG 3 Intranasal infection of MHV-3 impairs lung function. (a) Experimental design. (b) Pairwise comparison of ventilatory parameters recorded at 4 and 2 days before infection (−4 and −2 dpi) and at 3 dpi. Note that mice showed a significant increase in ventilation along with shortened respiratory cycles upon MHV-3 challenge. One-way repeated measures ANOVA plus Tukey's *post hoc* test were applied to assess differences between preinfection and postinfection periods ($n = 8$). (c) Analysis of pulmonary compliance showing reduced compliance and vital capacity in infected mice compared to that in mock-infected mice (unpaired *t* test; $n = 9$ to 11). Static compliance was calculated from the steepest point of the deflation part of the pressure-volume curve (right). ns, not significant ($P > 0.05$); *, $P < 0.05$; **, $P < 0.01$; ***, $P < 0.001$; ****, $P < 0.0001$.

clinical manifestations and death of the animals (as shown in Fig. 1b and c). Consistent with the liver damage, liver function was heavily impaired a 5 dpi, as seen by the high serum levels of alanine aminotransferase (ALT) and the reduced hepatic ability to metabolize indocyanine dye at this time point (Fig. 5). Other organs, such as the brain, small intestine, and colon, had minimal to mild leukocyte infiltration at 3 and 5 dpi and were much less affected than the liver (Fig. 6).

Furthermore, in view of recent evidence pointing to the high susceptibility of the testes to both SARS-CoV and SARS-CoV-2 infection (23, 24), we evaluated whether MHV-3 could trigger testicular damage. Interestingly, the percentage of altered seminiferous tubules increased significantly after inoculation. The altered sites displayed epithelium sloughing, elevated germ cell apoptosis, and retention of residual bodies (Fig. 6c and d). Also, there appeared to be an increase in the volumetric density of blood vessels and lymph space in the testis interstitium of infected mice (Fig. 6d to f), although such changes did not attain statistical significance. Together, these results indicate that intranasal inoculation of MHV-3 triggers multisystem changes beyond the transient lung damage.

TNF signaling abrogation significantly reduces lung injury and improves survival in MHV-3-infected mice. Increasing concentrations of TNF have previously been associated with tissue damages triggered by MHV and human coronaviruses and are currently thought to aggravate COVID-19 severity (6, 25–27). Once this cytokine was

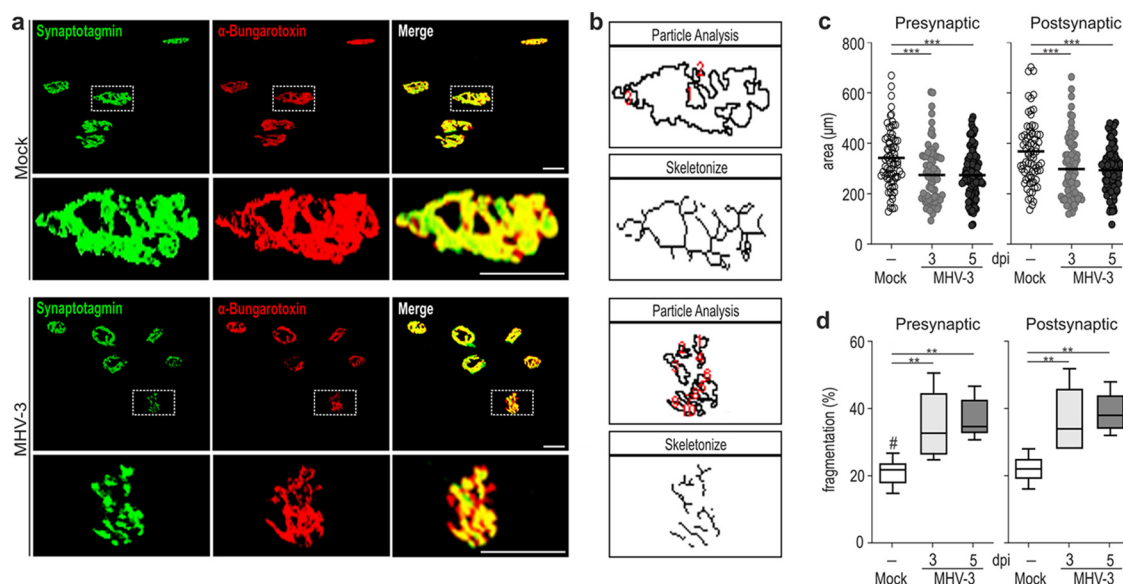


FIG 4 Neuromuscular junctions (NMJs) from diaphragm muscle are smaller and more fragmented in MHV-3-infected mice. (a) Three-dimensional confocal images from whole-mount diaphragm showing presynaptic (green) and postsynaptic terminals (red) at NMJs following 3 days of infection. Bar, 50 μm . (b) Representative images from skeletonization and particle analysis of the NMJ highlighted in figure a by dotted squares. Red numbers indicate fragmentation points. (c) Quantification of the area occupied by presynaptic and postsynaptic terminals. In total, 125 NMJs per group were considered in this analysis, and the values from infected animals were compared with those from mock controls by one-way ANOVA plus Dunnett's multiple-comparison test. (d) Quantification of the fragmentation percentages found in presynaptic and postsynaptic endings identified by particle analysis. Assessed by one-way ANOVA plus Dunnett's multiple-comparison test ($n = 5$). *, $P < 0.05$; **, $P < 0.01$; ***, $P < 0.001$; ****, $P < 0.0001$.

found here along with other proinflammatory mediators at higher levels within the lung of infected mice (Fig. 2g), we next interrogated the contribution of TNF signaling to the respiratory pathogenesis of MHV-3 infection. To this end, we intranasally infected mice genetically deficient for TNF receptor type 1 (TNFR1, also known as p55) with 10^3 PFU of MHV-3 and compared them with wild type (WT) mice. Strikingly, TNFR1 knockout (KO) mice were protected from abrupt weight loss and lethality, with 100% of mice surviving by the end of the 14-day follow-up period (Fig. 7a and b). The progressive leukopenia and thrombocytopenia phenotype observed in infected WT mice were not found in TNFR1 KO mice (Fig. 7c). Moreover, compared to the WT group, mice in the TNFR1 KO group had significantly lower viral loads (Fig. 7d), inflammation, and injury in their lungs (Fig. 7e to g).

To verify whether such a protective profile against MHV-3 could also be achieved using pharmacological approaches, WT mice were first infected intranasally with 10^3 PFU and then treated with etanercept, a selective TNF inhibitor (Fig. 8a). Regardless of the treatment route, etanercept did not prevent, but delayed, body weight loss (Fig. 8b). Similar findings were seen when survival rates were compared among groups, with etanercept-treated mice living 3 days longer on average than the untreated ones (vehicle group) (Fig. 8c). It is worth noting that both the local and systemic treatments with etanercept were capable of inhibiting MHV-3 replication in the lungs, with infectious viruses no longer detected in the majority of animals (Fig. 8d). Consistently, the inflammation-associated lung damage and overproduction of proinflammatory cytokines triggered by MHV-3 infection were substantially prevented with etanercept treatment, irrespective of the route of administration (Fig. 8e to g). Taken together, these findings reinforce an important contribution of the TNF pathway to the pathogenesis of respiratory coronavirus infection in mice.

Blocking TNF decreases SARS-CoV-2 replication and related cellular damage and proinflammatory cytokine production in human lung cells. We next evaluated the effects of etanercept treatment upon SARS-CoV-2 infection *in vitro*. For this, the human epithelial lung cell line Calu-3 was infected with SARS-CoV-2 and then treated

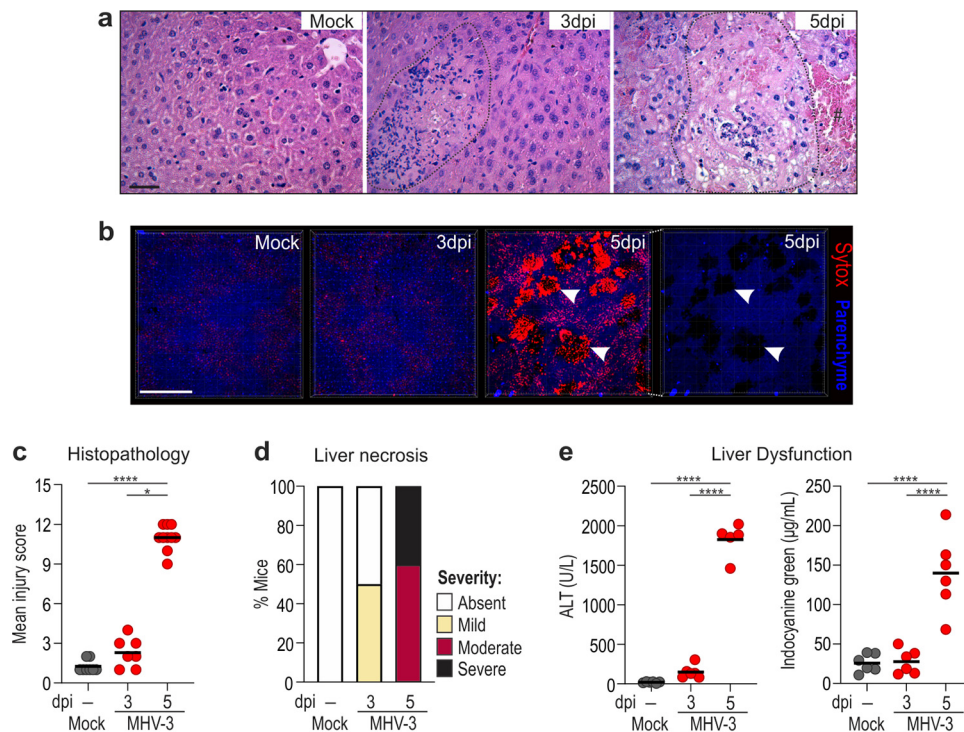


FIG 5 MHV-3 triggers liver dysfunction following 5 days of infection. (a) H&E staining of liver sections showing significant signs of tissue damage at 3 dpi and especially at 5 dpi. Areas morphologically compatible with necrosis were indicated by dotted circles. #, hemorrhage. Bar, 50 μ m. (b) Z-stack reconstruction showing extracellular DNA deposition in necrotic areas (arrowheads) identified by Sytox staining (in red). Autofluorescence (blue) was used to highlight the liver parenchyma. Bar, 300 μ m. (c) Mean injury scores compared among groups by Kruskal-Wallis plus Dunn's *post hoc* test. (d) Percentage of mice in each group according to the necrosis severity ($n = 7$ to 10). (e) Estimation of liver dysfunction analyzed by serum concentration of alanine aminotransferase (ALT) and indocyanine green (ICG) dye. Statistical differences among groups were assessed by one-way ANOVA plus Tukey's *post hoc* test ($n = 5$ or 6). ns, not significant ($P > 0.05$); *, $P < 0.05$; **, $P < 0.01$; ***, $P < 0.001$; ****, $P < 0.0001$.

with etanercept at different concentrations (0.5, 1, 5, and 10 ng/ml) (Fig. 9a). The results showed that etanercept treatment reduced the SARS-CoV-2-mediated cellular damage in a dose-dependent manner (Fig. 9b). Etanercept at 5 and 10 ng/ml had also a slight but statistically inhibitory effect on SARS-CoV-2 (Fig. 9c). Moreover, the overproduction of TNF, IL-8, and IL-18 triggered by SARS-CoV-2 infection was significantly reduced in Calu-3 cells treated with etanercept (Fig. 9d). These results suggest that TNF blocking by pharmacologic approaches might also be beneficial against SARS-CoV-2 infection in human lung epithelial cells.

DISCUSSION

The recent emergence and continuing spread of SARS-CoV-2 all over the world have launched a race toward the establishment of suitable *in vivo* platforms for evaluating vaccines and antiviral agents against human betacoronavirus (17). Here, we showed that the murine betacoronavirus MHV-3, despite its hepatotropism, may serve as a prototype to recapitulate, in wild-type mice, the many aspects of the respiratory disease and systemic alterations seen in patients with moderate or severe COVID-19. MHV-3 efficiently replicated in the lungs of C57BL/6J mice and triggered a robust inflammatory response, including accumulation of neutrophils and macrophages/monocytes accompanied by augmented tissue concentrations of proinflammatory cytokines and chemokines.

MHV-3 induced major lung histopathological changes, including alveolar edema, hemorrhage, and fibrin thrombi, which translated to functional alterations. Others betacoronaviruses might trigger transient pneumonia in wild-type mice, including the murine strains MHV-1, MHV-A59, and MHV-S (20, 21), as well as mouse-adapted SARS-CoV-2

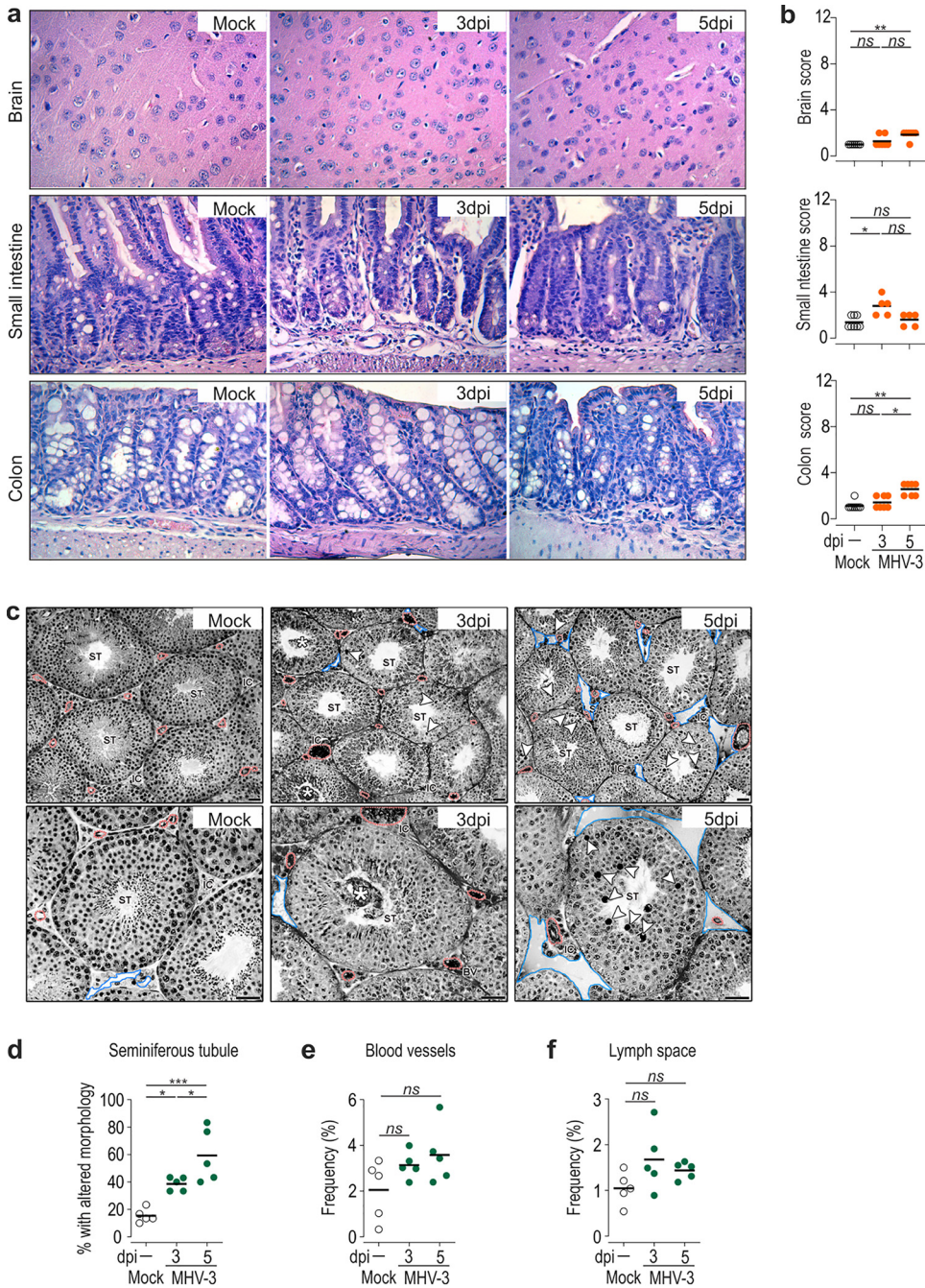


FIG 6 Extrapulmonary changes triggered by MHV-3 inoculated via the intranasal route. (a) H&E staining of the brain, small intestine, and colon sections showing mild signs of inflammatory injury in infected mice. Original magnification, $\times 400$. (b) Mean injury scores compared among groups by Kruskal-Wallis plus Dunn's *post hoc* test ($n = 5$ or 6). (c) Toluidine blue staining of testicular cross sections showing morphological alterations in infection groups. ST, seminiferous tubule; IC, intertubular compartment; *, epithelium sloughing. Arrowheads indicate germ cell apoptosis, reddish lines indicate blood vessels, and bluish lines indicate lymph space. Bar, $50 \mu\text{m}$. (d and e) Comparative morphometric analysis conducted in the tubular (d) and intratubular (e and f) compartments of mock versus MHV-3-infected mice. Assessed by one-way ANOVA plus Tukey's *post hoc* test (mean \pm SEM; $n = 5$). ns, not significant ($P > 0.05$); *, $P < 0.05$; **, $P < 0.01$; ***, $P < 0.001$; ****, $P < 0.0001$.

strains (15, 16); however, their impact on respiratory mechanics has scarcely been evaluated. Here, we showed that pulmonary ventilation was increased in MHV-3-infected mice supported by an augmented respiratory frequency (i.e., tachypnea) without significant alteration in tidal volume. The augmented ventilation may be a result of the hypoxemia-induced ventilatory reflex response, mediated by chemoreceptors (28). Although

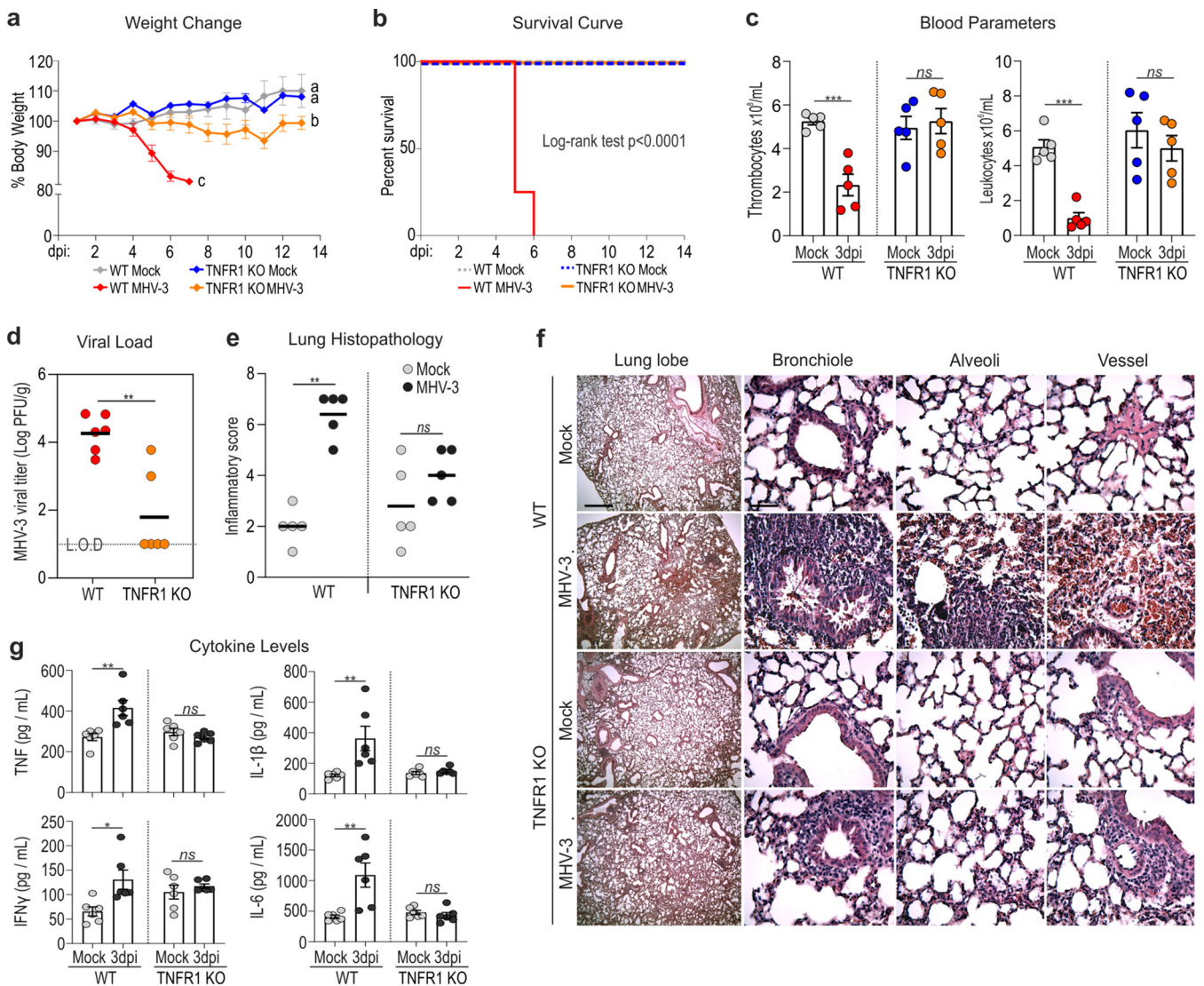


FIG 7 Genetic depletion of TNFR1 prevents MHV-3-mediated lung damage and death in mice. (a) Profile of body weight change in wild-type (WT) and TNFR1 knockout (KO) mice following 14 days of MHV-3 inoculation. Different letters represent statistically significant differences ($P < 0.05$) among groups assessed by two-way repeated-measures ANOVA plus Sidak's multiple-comparison test (mean \pm SEM; $n = 6$ to 8). (b) Kaplan-Meier survival curve of WT and TNFR1 KO mice upon infection ($n = 6$ to 8). (c) Blood analysis showing that the MHV-mediated thrombocytopenia and leukopenia in the WT do not occur in TNFR1 KO mice. Mean \pm SEM assessed by unpaired t test ($n = 5$). (d) Comparison of the viral load determined by plaque assay in WT versus TNFR1 KO mice at 3 days after infection. The data were presented as \log_{10} PFU per gram of tissue and assessed by Mann-Whitney test ($n = 6$). LOD, limit of detection. (e, f) Comparative histopathology of lungs from mock and infection groups (at 3 dpi) in relation to the mouse genotype. Statistical comparison among groups were made using the Mann-Whitney test ($n = 5$). Bars, 450 μm (low magnification) and 50 μm (high magnification). (g) Intrapulmonary concentration of TNF, IFN- γ , IL-6, and IL-1 β cytokines determined ELISA. Note that TNFR1 KO mice were prevented from the MHV-related overproduction of proinflammatory cytokines. Comparisons between mock versus infected mice were assessed by unpaired t test (mean \pm SEM; $n = 5$ or 6). ns, not significant ($P > 0.05$); *, $P < 0.05$; **, $P < 0.01$; ***, $P < 0.001$; ****, $P < 0.0001$.

we have not directly measured arterial blood gases, the lung pathologies of infected mice (alveolar edema, hyperemic vessels, and the presence of vessels with thrombi) strongly suggest deficits in gas exchange, provoked by dysfunctional diffusion and ventilation-to-perfusion ratio. The breathing pattern found in the infected mice, i.e., tachypnea-mediated increased ventilation, was well correlated with alterations of the mechanical properties of the respiratory system. Infected mice presented lower respiratory compliance that is suggestive of restrictive lung dysfunction. This sort of alteration is also described at least in some COVID-19 patients (29). From the viewpoint of respiratory work, a stiffened system (low compliance) augments the elastic work of breathing, and hence, increasing ventilation by a large tidal volume is energetically expansive and tachypnea is the prevailing breathing pattern in these circumstances (30, 31).

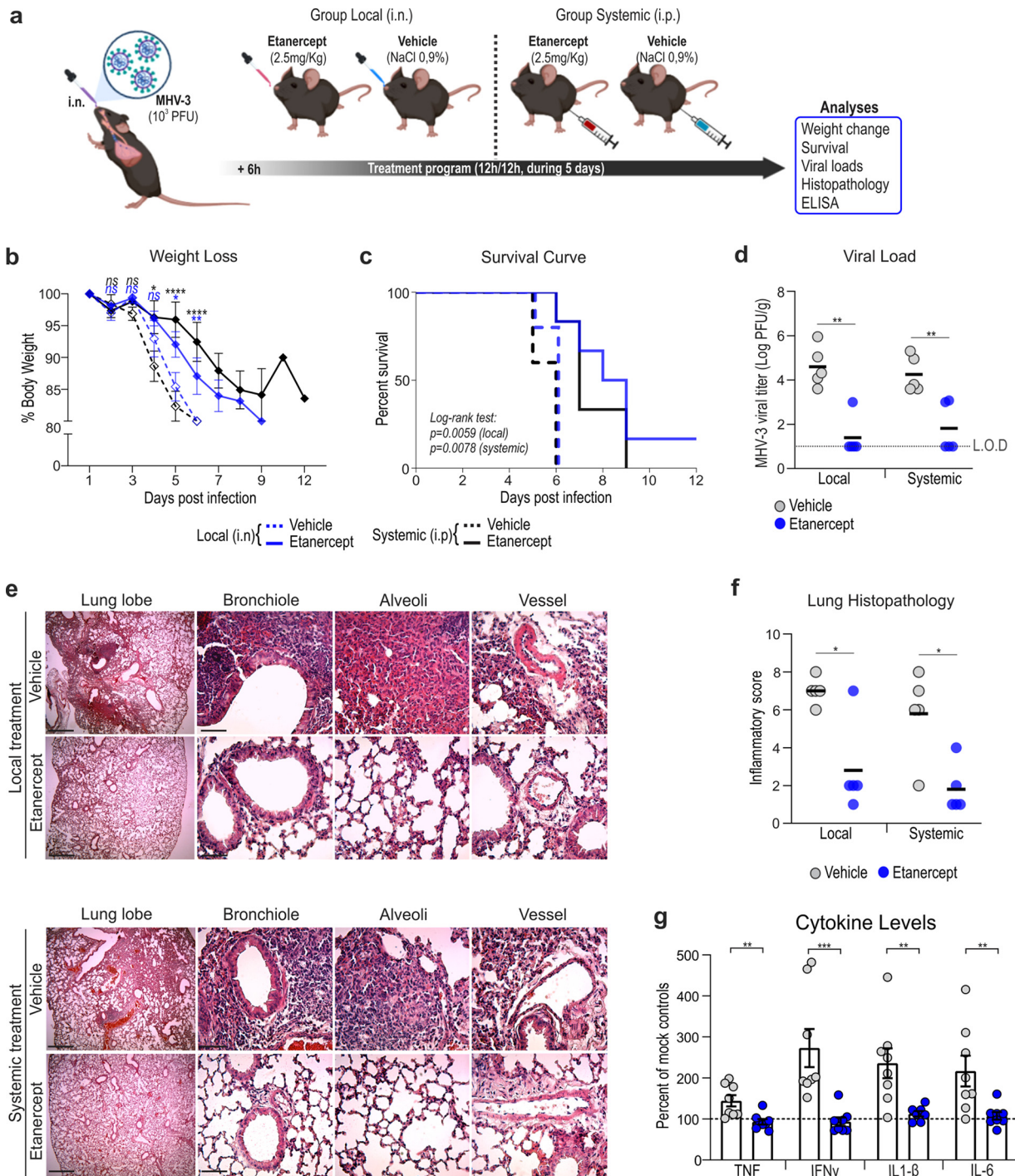


FIG 8 Pharmacologic blockade of TNF cytokine inhibits MHV-3 replication and inflammation-associated injury in the lungs of WT mice. (a) Experiment design. Following 24 h of MHV-3 inoculation, the animals received 2 mg/kg of etanercept or saline (vehicle) twice daily via the intranasal (i.n.; local treatment) or intraperitoneal (i.p.; systemic treatment) route. Treatment schedule was kept for 10 days in a group of animals to assess body weight change and lethality, whereas in another group, samples were collected at 3 dpi. (b) Profile of body weight change among groups. Differences between vehicle and etanercept groups were assessed according to the treatment route by two-way repeated measures ANOVA plus Sidak's multiple-comparison test (mean \pm SEM; $n = 8$). (c) Kaplan-Meier survival analysis of MHV-3-infected mice treated with etanercept versus vehicle controls ($n = 8$). (d) Viral load determined by plaque assay at 3 dpi in the lung of MHV-3-infected mice treated or not with etanercept. Statistical differences were assessed using the Mann-Whitney test ($n = 5$). LOD, limit of detection. (e) H&E staining of lung sections showing reduction of inflammation-associated injury signs in etanercept group versus vehicle controls at 3 dpi. Bar, 50 μ m. (f) Comparative histopathology of lungs according to groups (Mann-Whitney test; $n = 5$). (g) Concentrations of TNF, IFN- γ , IL-1 β , and IL-6 measured by ELISA in the lung of MHV-3-infected mice treated or not with etanercept. The values were normalized to the mock group and presented as percentage of mock controls (mean \pm SEM). Assessed by Mann-Whitney test. $n = 7$ or 8. ns, not significant ($P > 0.05$); *, $P < 0.05$; **, $P < 0.01$; ***, $P < 0.001$; ****, $P < 0.0001$.

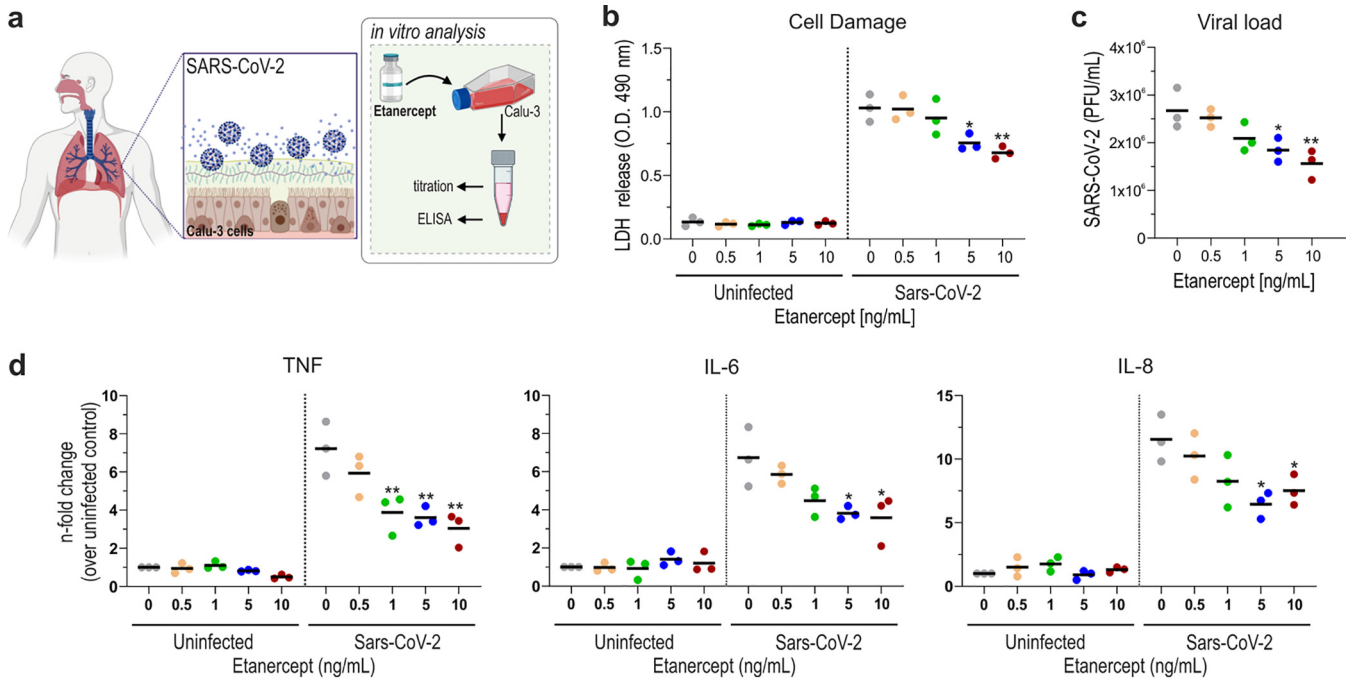


FIG 9 TNF blocking decreases SARS-CoV-2 replication and related cellular damage in human lung epithelial cells. (a) Experiment design. (b) Measurement of cell damage by dosing lactate dehydrogenase (LDH) levels released in cell supernatant of Calu-3 cells treated or not with different concentration of etanercept. (c) Changes in SARS-CoV-2 viral load determined in Calu-3 cells supernatants after treatment with increasing doses of etanercept. (d) ELISA showing lower concentrations of TNF, IL-6, and IL-8 in infected Calu-3 cells following etanercept treatment. Values from each dose group were compared to those from untreated controls by one-way ANOVA plus Dunnett’s multiple-comparison test. $n = 3$ independent experiments. *, $P < 0.05$; **, $P < 0.01$; ***, $P < 0.001$; ****, $P < 0.0001$.

Moreover, the infection-elicited symptoms in mice described here, fever and tachypnea, recapitulate symptoms described in some COVID-19 patients (32, 33).

It is noteworthy that after inducing pulmonary changes, MHV-3 spread to multiple organs and triggered a systemic and lethal disease. Although the host receptor used for virus entry differs between murine and human coronaviruses (34, 35), the dissemination of MHV-3 to extrapulmonary sites and the subsequent systemic hyperinflammation with high circulating levels of TNF, IFN- γ , IL-1- β , and IL-6 may provide a substantial platform to understand the mechanisms underlying the systemic inflammatory response syndrome (SIRS) and multiple organ failure (14, 36).

TNF has an important role in the coordination and development of most overexuberant inflammatory responses (6, 25, 26), and its inhibition can alleviate acute lung injury caused by severe respiratory syncytial virus and influenza virus (37, 38). During betacoronavirus infection, the overt TNF release can act synergically with IFN- γ and trigger robust inflammatory cell death (39, 40). Increasing studies in both MHV and SARS-CoV-2 have demonstrated that overt proinflammatory release, including TNF, is mediated by the host Toll-like receptor (TLR2)-Myd88 cascade (26, 41). Therefore, targeting either TNF or TLR2 blockade may provide substantial protection against the pathogenesis of coronavirus infection (39, 41). TNF has already been described as an important cytokine involved in inducing liver damage after intraperitoneal MHV-3 infection in mice (27). In this work, TNF was also associated with the induction of lung damage after intranasal infection with MHV-3. We showed that TNFR1 KO infected mice were fully protected from lung tissue injury and death. In line with this, treating infected wild-type mice with etanercept, a selective TNF inhibitor, mitigated the MHV-3-induced cytokine release and tissue damage in lungs. Moreover, we have shown that etanercept can also significantly decrease the cellular damage and proinflammatory cytokine release triggered by SARS-CoV-2 infection, *in vitro*. Although this preliminary result needs to be further confirmed by distinct *in vitro* and *in vivo* models of SARS-CoV-2 infection, it suggests that TNF blocking may alleviate the pathogenesis of betacoronavirus infection.

In summary, MHV-3 intranasal infection produced pathological features of severe acute respiratory syndrome in wild-type mice and translated into efficient virus replication in the lungs, induction of inflammation-associated tissue damage, and functional impairment of the respiratory function. Moreover, following respiratory manifestations, MHV-3 spread to distant organs and led to systemic inflammation and death, which enable the use of this mouse model for studying betacoronavirus-induced systemic alterations. Akin to other animal models already proposed for COVID-19 study, the MHV-3 model has limitations. One of them is the difference in the host cell receptor used for viral entry. All MHV strains uses the CEACAM-1 receptor (34), whereas SARS-CoV-2 uses ACE2 (35), which may preclude studies of viral entry or drugs that act on this stage of the replication cycle. Another important limitation is the strong viral tropism to extrapulmonary sites following 3 days of infection, which shortens the time window to assess unique pulmonary changes caused by MHV infection. In particular, the liver was severely affected at 5 dpi, at which necrotic areas could be frequently seen in the parenchyma. Although signs of liver injury (e.g., elevated levels of aminotransferases) have frequently been reported for COVID-19 patients and may be associated with disease severity (42), the MHV-induced hepatic changes seem to be greater in magnitude than those triggered by SARS-CoV-2. Thus, caution must be given to using the proposed model to understand the gastrointestinal manifestations of human betacoronavirus infections. Similarly, drugs that rely on the metabolism by hepatic enzymes should have their action limited at late time points of MHV-3 infection.

MATERIALS AND METHODS

Cells, viruses, and plaque assay. L929 (ATCC CCL-1), Vero E6 (ATCC CRL-1586), and Calu-3 (ATCC HTB-55) cells were cultured under a controlled atmosphere (37°C and 5% CO₂) in high-glucose Dulbecco's modified Eagle's medium (DMEM) (Vero and L929) or minimal essential medium (MEM) (Calu-3) supplemented with 7% fetal bovine serum (FBS), 100 U/ml penicillin, and 100 µg/ml streptomycin. The MHV-3 strain was provided and sequenced (GenBank accession no. [MW620427.1](#); see reference 43) by Clarice Weis Arns and Ricardo Durães-Carvalho from the Universidade Estadual de Campinas (UNICAMP, Brazil), and propagated in L929 cells. SARS-CoV-2 was expanded in Vero E6 cells from an isolate contained on a nasopharyngeal swab obtained from a confirmed case of COVID-19 in Rio de Janeiro, Brazil (GenBank accession no. [MT710714](#)), according to WHO guidelines. For viral titration, 100 µl of serially diluted virus suspension, plasma samples, and tissue homogenates (1:9 tissue to DMEM) were inoculated onto a confluent monolayer of L929 cells (for MHV-3) or Vero E6 cells (for SARS-CoV-2) grown in 24-well plates. After gentle shaking for 1 h (4 × 15 min), samples were removed and replaced with the overlay medium (DMEM containing 0.8% carboxymethylcellulose, 2% FBS, and 1% penicillin-streptomycin-glutamine) and kept for 2 days (for MHV-3) or 3 days (for SARS-CoV-2), at 37°C and 5% CO₂. Then, cells were fixed with 10% neutral buffered formalin (NBF) for 1 h and stained with 0.1% crystal violet. Virus titers were determined as PFU.

Mouse strains. Animal experimental procedures were carried out with mixed groups (males and females) of mice aged 6 to 7 weeks and received the approval of the Ethical Committee for Animal Experimentation of the Universidade Federal de Minas Gerais (UFMG) (process no. 190/2020). Wild-type C57BL/6 (Central Animal House of the UFMG) and TNF receptor knockout mice (TNFRp55^{-/-}, stock no. 002818; Jackson Laboratories) were housed in individually ventilated cages placed in an animal care facility at 24°C ± 2°C on a 12-h light/12-h dark cycle, receiving *ad libitum* access to water and food.

MHV-3 infection. Mice were lightly anesthetized (ketamine [50 mg/kg]-xylazine [5 mg/kg], intraperitoneally [i.p.]) and received an intranasal inoculation of 30 µl sterile saline solution, loaded or not (mock controls) with MHV-3 at different concentrations (3 × 10¹ to 3 × 10⁴ PFU). Signs of disease, including ruffled fur, back arching, weight loss, facial edema, and lack of activity were monitored daily for up to 14 days postinoculation (dpi).

Sample collection. Following anesthesia (ketamine [80 mg/kg]-xylazine [10 mg/kg], i.p.), the animals were euthanized by cervical dislocation, and blood samples were collected from the abdominal vena cava and analyzed. The lungs were then harvested, and the right lobes were snap-frozen in liquid nitrogen, whereas the left lobes were fixed in 10% neutral buffered formalin, unless otherwise mentioned. Formalin-fixed and frozen fragments of other target tissues were also collected for additional analyses.

Hematological evaluation. The number of circulating thrombocytes and leukocytes was determined in blood samples using the a Celltac MEK-6500K hemocytometer (Nihon Kohden).

Histopathology. Formalin-fixed and paraffin-embedded (FFPE) tissues were sectioned into 5-µm-thickness slices, stained with hematoxylin and eosin (H&E), and examined under light microscopy. The inflammation-mediated injury in mouse lungs was determined by a pathologist (C.M.Q.-J.) who was blind to the experimental conditions, employing a scoring system encompassing (i) airway inflammation (up to 4 points), (ii) vascular inflammation (up to 4 points), (iii) parenchyma inflammation (up to 5 points), and general neutrophil infiltration (up to 5 points) (44). Histopathological assessments were also performed in FFPE samples of liver, brain, small intestine, and colon, following previously established

criteria (45–48). For testis analysis, the tissue was fixed by immersion in Bouin's solution, embedded in glycol methacrylate resin, sectioned at 3- μ m thickness, and then stained with toluidine blue prior to stereological and morphometric assessments, as described previously (49).

Cytokine and chemokine dosage. Mouse lung homogenates were acquired by homogenizing 40 mg of frozen tissue in 400 ml of chilled cytokine extraction buffer (100 mM Tris [pH 7.4], 150 mM NaCl, 1 mM EGTA, 1 mM EDTA, 1% Triton X-100, 0.5% sodium deoxycholate, and 1% protease inhibitor cocktail). After centrifugation (14,000 \times g, 15 min, 4°C), the supernatant was collected and submitted to a dosage of TNF, IFN- γ , IL-10, IL-6, IL-1 β , IL-12 p70, CXCL-1, CCL-2, CCL-3, CCL-4, or CCL-5 using the mouse DuoSet enzyme-limited immunosorbent assay (ELISA) system (R&D Systems). Plasma concentrations of TNF, IFN- γ , IL-10, and IL-6 were also determined.

Immunofluorescence. Lung tissues were flushed with OCT/4% paraformaldehyde solution and processed for OCT embedding. The cryosections (15- μ m thickness) were permeabilized with phosphate-buffered saline (PBS)/0.5% Triton X-100, incubated for 1 h in the blocking solution (PBS containing 5% goat serum and 5 μ g/ml mouse BD Fc Block) and then labeled overnight at 4°C with the allophycocyanin (APC)-conjugated rat anti-mouse CD45 antibody (1:100 dilution, catalog no. 559864; BD Pharmingen). Cell nuclei were stained with 4',6-diamidino-2-phenylindole (DAPI; 1 μ g/ml, catalog no. D9542; Sigma-Aldrich). Fluorescent signals were evaluated by confocal microscopy using an inverted Nikon Eclipse Ti microscope coupled to an A1 scanning head.

Flow cytometry. Lungs were minced into small pieces and allowed to digest with gentle agitation (80 rpm, 37°C, 45 min) onto canonical tubes containing 5 ml of digestion buffer (0.5 mg/ml collagenase and 20 μ g/ml DNase diluted in RPMI medium). After, the cell suspension was passed through the cell strainer (pore size, 70 μ m; BD Biosciences, San Jose, CA), and the remaining erythrocytes were lysed with ACK buffer (Invitrogen, Carlsbad, CA). Cells (1 \times 10⁶) were blocked with mouse BD Fc Block (5 μ g/ml, catalog no. 553141; BD Pharmingen) and then stained using fluorescein-labeled monoclonal antibodies, as follows: Ly6G-BV421 (1:200, catalog no. 127627; BioLegend); CD45-fluorescein isothiocyanate (FITC) (1:200, catalog no. 5530801; BD Pharmingen); F4/80-phycoerythrin (PE)-Cyanine 7 (1:100, catalog no. 25-4801-82; Invitrogen); CD4-PE (1:100, catalog no. 100408; BioLegend); CD3-PerCP-Cyanine 5.5 (1:100, catalog no. 100218; BioLegend); CD8-allophycocyanin (APC) (1:100, catalog no. 17-0081-82; Invitrogen). The acquisition was carried out in a BD FACSCanto II cell analyzer and analyzed using FlowJo software (Tree Star, Ashland, OR).

Liver function analyses. Serum concentrations of alanine aminotransferase (ALT) and indocyanine green (ICG) were used to estimate the liver function status, as previously described (50). In addition, liver necrosis was evaluated by intravital microscopy after labeling free DNA. To this end, 20 min before *in vivo* imaging, mice received an intravenous injection of 1 mg Sytox orange diluted in 0.1 ml of sterile saline solution (51).

Measurement of body temperature. Ten days before MHV-3 inoculation, a group of 10 mice underwent surgery to implant a temperature probe (mini dataloggers; SubCue, Calgary, AB, Canada) into the abdominal cavity. The probes were programmed to start recording data at 7 a.m. on the fifth day after surgery. Upon starting, each animal's abdominal temperature was monitored every 10 min (sample rate) throughout the days that comprised pre- and postinfection procedures. On the fourth day postinfection, mice were euthanized, the dataloggers were collected, and the body temperature readings of each animal were downloaded and analyzed (SubCue Datalogger Software; Calgary, AB, Canada).

Pulmonary ventilation. The whole-body plethysmography method was employed to assess pulmonary ventilation (*in vivo*, freely moving animals) at 4 and 2 days before infection, as well as at 3 dpi. Mice were placed in a cylindrical plethysmography chamber flushed with room air (1,000 ml \cdot min⁻¹) and allowed to move freely and acclimate for at least 30 min. To measure pulmonary ventilation, the chamber was totally closed and airflow was stopped for a short period (~2 min) while the breathing-related pressure oscillations were detected using a differential pressure transducer, amplified (MLT141 spirometer, PowerLab; AdInstruments, NSW, Australia), and recorded with LabChart v.7 software (AdInstruments, NSW, Australia). The ventilation was calculated as the product of the tidal volume (ml body temperature and pressure, saturated [BTPS] \cdot g⁻¹; see reference 52) and respiratory frequency (breath cycles \cdot min⁻¹), corrected by the body weight (g). From the ventilatory recording traces, the inspiration and expiration time, as well as total respiratory cycle duration, were also calculated.

Respiratory mechanics. Mice were divided into two groups (mock $n = 9$ and infected $n = 11$) and 3 days postinfection animals were deeply anesthetized until respiratory arrest. Mice were tracheostomized and a polyethylene tube (P50) was inserted into the trachea. The pressure-volume curve was made by injecting air volume in a stepwise manner (using the 3-ml glass syringe), with 0.1-ml increments until intratracheal pressure peaked at approximately 35 cmH₂O. In the deflation limb, the system was deflated in the same volume steps until the pressure reached approximately -15 cmH₂O and finally inflated again to resting lung volume. Signals were acquired and recorded on the PowerLab software (LabChart v. 7; AdInstruments, NSW, Australia). The vital capacity was determined by maximal inflation (lung volume at 35 cmH₂O), and the static compliance of the total respiratory system (expressed as ml/cmH₂O) was measured at the steepest point of the deflation limb of the pressure-volume curve.

Neuromuscular junction analysis of diaphragm muscle. Whole-mount diaphragms were used to evaluate changes in neuromuscular junctions (NMJs) of MHV-3-infected mice and mock controls. Sample processing and labeling of NMJs were performed based on a previous protocol (53). The presynaptic and postsynaptic terminals were stained using the monoclonal anti-synaptotagmin antibody (1:250 dilution, catalog no. 3H2 2D7; Developmental Studies Hybridoma Bank) and the tetramethylrhodamine-conjugated α -bungarotoxin (1:1,000 dilution, catalog no. T1175; Invitrogen), respectively. After Z-stack imaging in a Zeiss LSM 880 confocal microscope, 25 NMJs per animal were assessed by particle analysis to estimate the fragmentation index at pre- and postsynaptic endings (54).

Etanercept treatment. For *in vivo* TNF inhibition, C57BL/6J WT mice were intranasally inoculated with 1×10^3 PFU of MHV and received 2.5 mg/kg of etanercept (Enbrel; Pfizer) twice a day delivered in 30 μ l sterile saline solution via the nasal route (local treatment scheme) or intraperitoneally (systemic treatment scheme). Treatments started following 6 h after infection and lasted until 6 dpi. The vehicle groups received only saline solution.

TNF inhibition was also tested *in vitro* against SARS-CoV-2. To this end, Calu-3 cells were seeded onto 24-well plates and infected with SARS-CoV-2 (multiplicity of infection [MOI] 0.1). The control group was kept uninfected. After 1 h of viral adsorption, the medium containing virus was replaced for fresh medium loaded with increasing concentrations of Etanercept (0.5, 1, 5, and 10 ng/ml). Following 48 h of treatment, the Calu-3 supernatant was collected for measuring virus load as well as the concentration of target cytokines and lactate dehydrogenase (LDH).

Statistical analyses. Prism 8.0 software (GraphPad) was used for statistical analysis. First, data distribution was assessed by the Shapiro-Wilk test and Q-Q plots. Parametric comparisons between two or more groups were done using Student's *t* test or one-way analysis of variance (ANOVA), respectively, or by using a Mann-Whitney or Kruskal-Wallis test to assess differences between two or more nonparametric data sets. Survival rates among groups were determined by Kaplan-Meier survival analysis. Finally, the body weight changes triggered by MHV-3 were compared among groups by two-way repeated-measures ANOVA. Data are presented as mean \pm standard error of the mean (SEM). Differences with a *P* value of <0.05 were considered statistically significant.

ACKNOWLEDGMENTS

This work was financially supported by grants from Coordenação de Aperfeiçoamento de Pessoal de Nível Superior–CAPES/Brazil (grant 88887.507173/2020-00 to M.M.T.), JBS-INVITARE/Brazil (grant 27991 to M.M.T.), Fundação de Amparo à Pesquisa do Estado de São Paulo–FAPESP/Brazil (grant 2019/01255-9 to R.D.-C.), a Ferring COVID-19 Investigational Grant (grant FIN0042393 to G.M.J.C.), and the L'Oréal-Unesco-ABC For Women in Science Program (grant to V.V.C.). This work also received support from the National Institute of Science and Technology in Dengue and Host-Microorganism Interaction (INCT em Dengue), sponsored by the Conselho Nacional de Desenvolvimento Científico e Tecnológico (CNPq; Brazil) and the Fundação de Amparo à Pesquisa do Estado de Minas Gerais (FAPEMIG; Brazil).

We also acknowledge Leda Quercia Vieira for the donation of the TNFR1 KO mice and Ilma Marçal de Souza for her technical assistance with experiments.

Author contributions were as follows. Study design: A.C.D.S.P.A., G.H.C.-S., C.M.Q.-J., L.C.D.O., L.P.D.S., M.M.T., G.S.F.D.S., and V.V.C. Performed experiments: A.C.D.S.P.A., G.H.C.-S., C.M.Q.-S., L.C.D.O., L.D.S.B.L., J.C.P., F.R.O.D.S., I.D.M.C., I.B.P., D.C.T., P.G.B.-S., P.A.C.V., L.R.-O., M.M.A., A.F.A.F., N.T.W., A.C.F., J.R.T., and A.C. Data analysis: A.C.D.S.P.A., G.H.C.S., L.P.D.S., G.S.F.D.S., G.M.J.C., C.G., T.M.L.S., R.D.-C., and V.V.C. Intellectual, technical and resource support: M.M.T., C.A.D., C.W.A., P.P.G.G., G.B.D.M., T.M.L.S., M.D.M.P., and B.R.B. Wrote the first draft of the paper: A.C.D.S.P.A., G.H.C.-S., C.M.Q.-J., L.C.D.O., L.P.D.S., G.S.F.D.S., C.G., and V.V.C. All authors reviewed and approved the final version of the manuscript.

We declare no competing financial interest in relation to this work.

REFERENCES

- Cui J, Li F, Shi ZL. 2019. Origin and evolution of pathogenic coronaviruses. *Nat Rev Microbiol* 17:181–192. <https://doi.org/10.1038/s41579-018-0118-9>.
- Boni MF, Lemey P, Jiang X, Lam TTY, Perry BW, Castoe TA, Rambaut A, Robertson DL. 2020. Evolutionary origins of the SARS-CoV-2 sarbecovirus lineage responsible for the COVID-19 pandemic. *Nat Microbiol* 5: 1408–1417. <https://doi.org/10.1038/s41564-020-0771-4>.
- Wang W, Lin XD, Zhang HL, Wang MR, Guan XQ, Holmes EC, Zhang YZ. 2020. Extensive genetic diversity and host range of rodent-borne coronaviruses. *Virus Evol* 6:veaa078. <https://doi.org/10.1093/ve/veaa078>.
- Lu R, Zhao X, Li J, Niu P, Yang B, Wu H, Wang W, Song H, Huang B, Zhu N, Bi Y, Ma X, Zhan F, Wang L, Hu T, Zhou H, Hu Z, Zhou W, Zhao L, Chen J, Meng Y, Wang J, Lin Y, Yuan J, Xie Z, Ma J, Liu WJ, Wang D, Xu W, Holmes EC, Gao GF, Wu G, Chen W, Shi W, Tan W. 2020. Genomic characterisation and epidemiology of 2019 novel coronavirus: implications for virus origins and receptor binding. *Lancet* 395:565–574. [https://doi.org/10.1016/S0140-6736\(20\)30251-8](https://doi.org/10.1016/S0140-6736(20)30251-8).
- Huang C, Wang Y, Li X, Ren L, Zhao J, Hu Y, Zhang L, Fan G, Xu J, Gu X, Cheng Z, Yu T, Xia J, Wei Y, Wu W, Xie X, Yin W, Li H, Liu M, Xiao Y, Gao H, Guo L, Xie J, Wang G, Jiang R, Gao Z, Jin Q, Wang J, Cao B. 2020. Clinical features of patients infected with 2019 novel coronavirus in Wuhan, China. *Lancet* 395: 497–506. [https://doi.org/10.1016/S0140-6736\(20\)30183-5](https://doi.org/10.1016/S0140-6736(20)30183-5).
- Del Valle DM, Kim-Schulze S, Huang HH, Beckmann ND, Nirenberg S, Wang B, Lavin Y, Swartz TH, Madduri D, Stock A, Marron TU, Xie H, Patel M, Tuballes K, Van Oekelen O, Rahman A, Kovatch P, Aberg JA, Schadt E, Jagannath S, Mazumdar M, Charney AW, Firpo-Betancourt A, Mendu DR, Jhang J, Reich D, Sigel K, Cordon-Cardo C, Feldmann M, Parekh S, Merad M, Gnjatic S. 2020. An inflammatory cytokine signature predicts COVID-19 severity and survival. *Nat Med* 26:1636–1643. <https://doi.org/10.1038/s41591-020-1051-9>.
- Gurumurthy CB, Quadros RM, Richardson GP, Poluektova LY, Mansour SL, Ohtsuka M. 2020. Genetically modified mouse models to help fight COVID-19. *Nat Protoc* 15:3777–3787. <https://doi.org/10.1038/s41596-020-00403-2>.
- Winkler ES, Bailey AL, Kafai NM, Nair S, McCune BT, Yu J, Fox JM, Chen RE, Earnest JT, Keeler SP, Ritter JH, Kang LI, Dort S, Robichaud A, Head R, Holtzman MJ, Diamond MS. 2020. SARS-CoV-2 infection of human ACE2-transgenic mice causes severe lung inflammation and impaired function. *Nat Immunol* 21:1327–1335. <https://doi.org/10.1038/s41590-020-0778-2>.

9. Dinnon KH, Leist SR, Schäfer A, Edwards CE, Martinez DR, Montgomery SA, West A, Yount BL, Hou YJ, Adams LE, Gully KL, Brown AJ, Huang E, Bryant MD, Choong IC, Glenn JS, Gralinski LE, Sheahan TP, Baric RS. 2020. A mouse-adapted model of SARS-CoV-2 to test COVID-19 countermeasures. *Nature* 586:560–566. <https://doi.org/10.1038/s41586-020-2708-8>.
10. Shi J, Wen Z, Zhong G, Yang H, Wang C, Huang B, Liu R, He X, Shuai L, Sun Z, Zhao Y, Liu P, Liang L, Cui P, Wang J, Zhang X, Guan Y, Tan W, Wu G, Chen H, Bu Z, Bu Z. 2020. Susceptibility of ferrets, cats, dogs, and other domesticated animals to SARS-coronavirus 2. *Science* 368:1016–1020. <https://doi.org/10.1126/science.abb7015>.
11. Rockx B, Kuiken T, Herfst S, Bestebroer T, Lamers MM, Munnink BBO, De Meulder D, Van Amerongen G, Van Den Brand J, Okba NMA, Schipper D, Van Run P, Leijten L, Sikkema R, Verschoor E, Verstrepen B, Bogers W, Langermans J, Langermans J, Drosten C, Van Vliissingen MF, Fouchier R, De Swart R, Koopmans M, Haagmans BL. 2020. Comparative pathogenesis of COVID-19, MERS, and SARS in a nonhuman primate model. *Science* 368:1012–1015. <https://doi.org/10.1126/science.abb7314>.
12. Sia SF, Yan LM, Chin AWH, Fung K, Choy KT, Wong AYL, Kaewpreedee P, Perera RAPM, Poon LLM, Nicholls JM, Peiris M, Yen HL. 2020. Pathogenesis and transmission of SARS-CoV-2 in golden hamsters. *Nature* 583:834–838. <https://doi.org/10.1038/s41586-020-2342-5>.
13. Gu H, Chen Q, Yang G, He L, Fan H, Deng YQ, Wang Y, Teng Y, Zhao Z, Cui Y, Li Y, Li XF, Li J, Zhang NN, Yang X, Chen S, Guo Y, Zhao G, Wang X, Luo DY, Wang H, Yang X, Li Y, Han G, He Y, Zhou X, Geng S, Sheng X, Jiang S, Sun S, Qin CF, Zhou Y. 2020. Adaptation of SARS-CoV-2 in BALB/c mice for testing vaccine efficacy. *Science* 369:1603–1607. <https://doi.org/10.1126/science.abc4730>.
14. Wang J, Shuai L, Wang C, Liu R, He X, Zhang X, Sun Z, Shan D, Ge J, Wang X, Hua R, Zhong G, Wen Z, Bu Z. 2020. Mouse-adapted SARS-CoV-2 replicates efficiently in the upper and lower respiratory tract of BALB/c and C57BL/6J mice. *Protein Cell* 11:776–782. <https://doi.org/10.1007/s13238-020-00767-x>.
15. Bao L, Deng W, Huang B, Gao H, Liu J, Ren L, Wei Q, Yu P, Xu Y, Qi F, Qu Y, Li F, Lv Q, Wang W, Xue J, Gong S, Liu M, Wang G, Wang S, Song Z, Zhao L, Liu P, Zhao L, Ye F, Wang H, Zhou W, Zhu N, Zhen W, Yu H, Zhang X, Guo L, Chen L, Wang C, Wang Y, Wang X, Xiao Y, Sun Q, Liu H, Zhu F, Ma C, Yan L, Yang M, Han J, Xu W, Tan W, Peng X, Jin Q, Wu G, Qin C. 2020. The pathogenicity of SARS-CoV-2 in hACE2 transgenic mice. *Nature* 583:830–833. <https://doi.org/10.1038/s41586-020-2312-y>.
16. Ehaideb SN, Abdullah ML, Abuyassin B, Bouchama A. 2020. Evidence of a wide gap between COVID-19 in humans and animal models: a systematic review. *Crit Care* 24:–594. <https://doi.org/10.1186/s13054-020-03304-8>.
17. Muñoz-Fontela C, Dowling WE, Funnell SGP, Gsell PS, Riveros-Balta AX, Albrecht RA, Andersen H, Baric RS, Carroll MW, Cavaleri M, Qin C, Crozier I, Dallmeier K, de Waal L, de Wit E, Delang L, Dohm E, Duprex WP, Falzarano D, Finch CL, Frieman MB, Graham BS, Gralinski LE, Guilfoyle K, Haagmans BL, Hamilton GA, Hartman AL, Herfst S, Kaptein SJF, Klimstra WB, Knezevic I, Krause PR, Kuhn JH, Le Grand R, Lewis MG, Liu WC, Maisonnasse P, McElroy AK, Munster V, Oreshkova N, Rasmussen AL, Rocha-Pereira J, Rockx B, Rodríguez E, Rogers TF, Salguero FJ, Schotsaert M, Stittelaar KJ, Thibaut HJ, Te Tseng C, Vergara-Alert J, et al. 2020. Animal models for COVID-19. *Nature* 586:509–515. <https://doi.org/10.1038/s41586-020-2787-6>.
18. De Albuquerque N, Baig E, Ma X, Zhang J, He W, Rowe A, Habal M, Liu M, Shalev I, Downey GP, Gorczynski R, Butany J, Leibowitz J, Weiss SR, McGillvray ID, Phillips MJ, Fish EN, Levy GA. 2006. Murine hepatitis virus strain 1 produces a clinically relevant model of severe acute respiratory syndrome in A/J mice. *J Virol* 80:10382–10394. <https://doi.org/10.1128/JVI.00747-06>.
19. Yang Z, Du J, Chen G, Zhao J, Yang X, Su L, Cheng G, Tang H. 2014. Coronavirus MHV-A59 infects the lung and causes severe pneumonia in C57BL/6 mice. *Virology* 463:393–402. <https://doi.org/10.1007/s12250-014-3530-y>.
20. Weiss SR, Leibowitz JL. 2011. Coronavirus pathogenesis, p 85–164. *In* Advances in virus research, 1st ed. Academic Press, Cambridge, MA.
21. Körner RW, Majjouti M, Alejandre Alcazar MA, Mahabir E. 2020. Of mice and men: the coronavirus MHV and mouse models as a translational approach to understand SARS-COV-2. *Viruses* 12:880. <https://doi.org/10.3390/v12080880>.
22. Shi Z, de Vries HJ, Vlaar APJ, van der Hoeven J, Boon RA, Heunks LMA, Ottenheim CAC, Dutch COVID-19 Diaphragm Investigators. 2021. Diaphragm pathology in critically ill patients with COVID-19 and postmortem findings from 3 medical centers. *JAMA Intern Med* 181:122–124. <https://doi.org/10.1001/jamainternmed.2020.6278>.
23. Chen L, Huang X, Yi Z, Deng Q, Jiang N, Feng C, Zhou Q, Sun B, Chen W, Guo R. 2021. Ultrasound imaging findings of acute testicular infection in patients with coronavirus disease 2019. *J Ultrasound Med* 40:1787–1788. <https://doi.org/10.1002/jum.15558>.
24. Ma X, Guan C, Chen R, Wang Y, Feng S, Wang R, Qu G, Zhao S, Wang F, Wang X, Zhang D, Liu L, Liao A, Yuan S. 2021. Pathological and molecular examinations of postmortem testis biopsies reveal SARS-CoV-2 infection in the testis and spermatogenesis damage in COVID-19 patients. *Cell Mol Immunol* 18:487–489. <https://doi.org/10.1038/s41423-020-00604-5>.
25. Haga S, Yamamoto N, Nakai-Murakami C, Osawa Y, Tokunaga K, Sata T, Yamamoto N, Sasazuki T, Ishizaka Y. 2008. Modulation of TNF- α -converting enzyme by the spike protein of SARS-CoV and ACE2 induces TNF- α production and facilitates viral entry. *Proc Natl Acad Sci U S A* 105:7809–7814. <https://doi.org/10.1073/pnas.0711241105>.
26. Jacques A, Bleau C, Turbide C, Beauchemin N, Lamontagne L. 2009. Macrophage interleukin-6 and tumour necrosis factor- α are induced by coronavirus fixation to Toll-like receptor 2/heparan sulphate receptors but not carcinoembryonic cell adhesion antigen 1a. *Immunology* 128:e181–e192. <https://doi.org/10.1111/j.1365-2567.2008.02946.x>.
27. Xu H, Li H, Cao D, Wu Y, Chen Y. 2014. Tumor necrosis factor α (TNF- α) receptor-1 is required for TNF- α -mediated fulminant virus hepatitis caused by murine hepatitis virus strain-3 infection. *Immunol Lett* 158:25–32. <https://doi.org/10.1016/j.imlet.2013.11.008>.
28. Vaporidi K, Akoumianaki E, Telias I, Goligher EC, Brochard L, Georgopoulos D. 2020. Respiratory drive in critically ill patients: pathophysiology and clinical implications. *Am J Respir Crit Care Med* 201:20–32. <https://doi.org/10.1164/rccm.201903-0596SO>.
29. Gattinoni L, Chiumello D, Caironi P, Busana M, Romitti F, Brazzi L, Camporota L. 2020. COVID-19 pneumonia: different respiratory treatments for different phenotypes? *Intensive Care Med* 46:1099–1102. <https://doi.org/10.1007/s00134-020-06033-2>.
30. Mortola JP. 2019. How to breathe? Respiratory mechanics and breathing pattern. *Respir Physiol Neurobiol* 261:48–54. <https://doi.org/10.1016/j.resp.2018.12.005>.
31. Robichaud A, Fereydoonzaad L, Limjunyawong N, Rabold R, Allard B, Benedetti A, Martin JG, Mitzner W. 2017. Automated full-range pressure-volume curves in mice and rats. *J Appl Physiol* (1985) 123:746–756. <https://doi.org/10.1152/jappphysiol.00856.2016>.
32. Zhao Y, Shang Y, Song W, Li Q, Xie H, Xu Q, Jia J, Li L, Mao H, Zhou X, Luo H, Gao Y, Xu A. 2020. Follow-up study of the pulmonary function and related physiological characteristics of COVID-19 survivors three months after recovery. *EclinicalMedicine* 25:100463. <https://doi.org/10.1016/j.eclinm.2020.100463>.
33. Poor HD, Ventetuolo CE, Tolbert T, Chun G, Serrao G, Zeidman A, Dangayach NS, Olin J, Kohli-Seth R, Powell CA. 2020. COVID-19 critical illness pathophysiology driven by diffuse pulmonary thrombi and pulmonary endothelial dysfunction responsive to thrombolysis. *Clin Transl Med* 10:3–7.
34. Blau DM, Turbide C, Tremblay M, Olson M, Létoirneau S, Michaliszyn E, Jothy S, Holmes KV, Beauchemin N. 2001. Targeted disruption of the Cea-cam1 (MHVR) gene leads to reduced susceptibility of mice to mouse hepatitis virus infection. *J Virol* 75:8173–8186. <https://doi.org/10.1128/jvi.75.17.8173-8186.2001>.
35. Hoffmann M, Kleine-Weber H, Schroeder S, Krüger N, Herrler T, Erichsen S, Schiergens TS, Herrler G, Wu NH, Nitsche A, Müller ACE, Drosten C, Pöhlmann S. 2020. SARS-CoV-2 cell entry depends on ACE2 and TMPRSS2 and is blocked by a clinically proven protease inhibitor. *Cell* 181:271–280.e8. <https://doi.org/10.1016/j.cell.2020.02.052>.
36. Lai CC, Ko WC, Lee PI, Jean SS, Hsueh PR. 2020. Extra-respiratory manifestations of COVID-19. *Int J Antimicrob Agents* 56:106024. <https://doi.org/10.1016/j.ijantimicag.2020.106024>.
37. Hussell T, Pennycook A, Openshaw PJM. 2001. Inhibition of tumor necrosis factor reduces the severity of virus-specific lung immunopathology. *Eur J Immunol* 31:2566–2573. [https://doi.org/10.1002/1521-4141\(200109\)31:9<2566::AID-IMMU2566>3.0.CO;2-L](https://doi.org/10.1002/1521-4141(200109)31:9<2566::AID-IMMU2566>3.0.CO;2-L).
38. Shi X, Zhou W, Huang H, Zhu H, Zhou P, Zhu H, Ju D. 2013. Inhibition of the inflammatory cytokine tumor necrosis factor- α with etanercept provides protection against lethal H1N1 influenza infection in mice. *Crit Care* 17:R301. <https://doi.org/10.1186/cc13171>.
39. Zheng M, Williams EP, Subbarao Malireddi RK, Karki R, Banoth B, Burton A, Webby R, Channappanavar R, Jonsson CB, Kanneganti TD. 2020. Impaired NLRP3 inflammasome activation/pyroptosis leads to robust inflammatory cell death via caspase-8/RIPK3 during coronavirus infection. *J Biol Chem* 295:14040–14052. <https://doi.org/10.1074/jbc.RA120.015036>.

40. Karki R, Sharma BR, Tuladhar S, Williams EP, Zalduondo L, Samir P, Zheng M, Sundaram B, Banoth B, Malireddi RKS, Schreiner P, Neale G, Vogel P, Webby R, Jonsson CB, Kanneganti TD. 2021. Synergism of TNF- α and IFN- γ Triggers inflammatory cell death, tissue damage, and mortality in SARS-CoV-2 infection and cytokine shock syndromes. *Cell* 184:149–168.e17. <https://doi.org/10.1016/j.cell.2020.11.025>.
41. Zheng M, Karki R, Williams EP, Yang D, Fitzpatrick E, Vogel P, Jonsson CB, Kanneganti TD. 2021. TLR2 senses the SARS-CoV-2 envelope protein to produce inflammatory cytokines. *Nat Immunol* 22:829–838. <https://doi.org/10.1038/s41590-021-00937-x>.
42. Wang Y, Liu S, Liu H, Li W, Lin F, Jiang L, Li X, Xu P, Zhang L, Zhao L, Cao Y, Kang J, Yang J, Li L, Liu X, Li Y, Nie R, Mu J, Lu F, Zhao S, Lu J, Zhao J. 2020. SARS-CoV-2 infection of the liver directly contributes to hepatic impairment in patients with COVID-19. *J Hepatol* 73:807–816. <https://doi.org/10.1016/j.jhep.2020.05.002>.
43. Garcia AB, De Moraes P, Rodrigues DM, Gilioli R, de Oliveira-Filho EF, Durães-Carvalho R, Weis Arns C. 2021. Coding-complete genome sequence of murine hepatitis virus strain 3 from Brazil. *Microbiol Resour Announc* 10:e00248-21. <https://doi.org/10.1128/MRA.00248-21>.
44. Horvat JC, Beagley KW, Wade MA, Preston JA, Hansbro NG, Hickey DK, Kaiko GE, Gibson PG, Foster PS, Hansbro PM. 2007. Neonatal chlamydial infection induces mixed T-cell responses that drive allergic airway disease. *Am J Respir Crit Care Med* 176:556–564. <https://doi.org/10.1164/rccm.200607-1005OC>.
45. Costa VV, Fagundes CT, Valadão DF, Cisalpino D, Dias ACF, Silveira KD, Kangussu LM, Ávila TV, Bonfim MRQ, Bonaventura D, Silva TA, Sousa LP, Rachid MA, Vieira LQ, Menezes GB, de Paula AM, Atrasheuskaya A, Ignatyev G, Teixeira MM, Souza DG. 2012. A model of DENV-3 infection that recapitulates severe disease and highlights the importance of IFN- γ in host resistance to infection. *PLoS Negl Trop Dis* 6:e1663. <https://doi.org/10.1371/journal.pntd.0001663>.
46. Costa VV, Del Sarto JL, Rocha RF, Silva FR, Doria JG, Olmo IG, Marques RE, Queiroz-Junior CM, Foureaux G, Araújo JMS, Cramer A, Real ALCV, Ribeiro LS, Sardi SI, Ferreir AJ, Machado FS, De Oliveira AC, Teixeira AL, Nakaya HI, Souza DG, Ribeiro FM, Teixeira MM. 2017. N-Methyl-D-aspartate (NMDA) receptor blockade prevents neuronal death induced by Zika virus infection. *mBio* 8:e00350-17. <https://doi.org/10.1128/mBio.00350-17>.
47. Arifa RDN, Madeira MFM, De Paula TP, Lima RL, Tavares LD, Menezes-Garcia Z, Fagundes CT, Rachid MA, Ryffel B, Zamboni DS, Teixeira MM, Souza DG. 2014. Inflammasome activation is reactive oxygen species dependent and mediates irinotecan-induced mucositis through IL-1 β and IL-18 in mice. *Am J Pathol* 184:2023–2034. <https://doi.org/10.1016/j.ajpath.2014.03.012>.
48. MacPherson BR, Pfeiffer CJ. 1978. Experimental production of diffuse colitis in rats. *Digestion* 17:135–150. <https://doi.org/10.1159/000198104>.
49. Costa GMJ, Lacerda SMSN, Figueiredo AFA, Leal MC, Rezende-Neto JV, França LR. 2018. Higher environmental temperatures promote acceleration of spermatogenesis *in vivo* in mice (*Mus musculus*). *J Therm Biol* 77:14–23. <https://doi.org/10.1016/j.jtherbio.2018.07.010>.
50. Nakagaki BN, Mafra K, de Carvalho É, Lopes ME, Carvalho-Gontijo R, de Castro-Oliveira HM, Campolina-Silva GH, de Miranda CDM, Antunes MM, Silva ACC, Diniz AB, Alvarenga DM, Lopes MAF, de Souza Lacerda VA, Mattos MS, Araújo AM, Vidigal PVT, Lima CX, Mahecha GAB, Madeira MFM, Fernandes GR, Nogueira RF, Moreira TG, David BA, Rezende RM, Menezes GB. 2018. Immune and metabolic shifts during neonatal development reprogram liver identity and function. *J Hepatol* 69:1294–1307. <https://doi.org/10.1016/j.jhep.2018.08.018>.
51. Marques PE, Oliveira AG, Pereira RV, David BA, Gomides LF, Saraiva AM, Pires DA, Novaes JT, Patrício DO, Cisalpino D, Menezes-Garcia Z, Leevy WM, Chapman SE, Mahecha G, Marques RE, Guabiraba R, Martins VP, Souza DG, Mansur DS, Teixeira MM, Leite MF, Menezes GB. 2015. Hepatic DNA deposition drives drug-induced liver injury and inflammation in mice. *Hepatology* 61:348–360. <https://doi.org/10.1002/hep.27216>.
52. Mortola JP, Frappell PB. 2013. Measurements of air ventilation in small vertebrates. *Respir Physiol Neurobiol* 186:197–205. <https://doi.org/10.1016/j.resp.2013.02.001>.
53. Valadão PAC, Gomes MPSM, Aragão BC, Rodrigues HA, Andrade JN, Garcias R, Joviano-Santos JV, Luiz MA, Camargo WL, Naves LA, Kushmerick C, Cavalcante WLG, Gallacci M, de Jesus ICG, Guatimosim S, Guatimosim C. 2018. Neuromuscular synapse degeneration without muscle function loss in the diaphragm of a murine model for Huntington's disease. *Neurochem Int* 116:30–42. <https://doi.org/10.1016/j.neuint.2018.03.007>.
54. Valadão PAC, de Aragão BC, Andrade JN, Magalhães-Gomes MPS, Foureaux G, Joviano-Santos JV, Nogueira JC, Ribeiro FM, Tapia JC, Guatimosim C. 2017. Muscle atrophy is associated with cervical spinal motoneuron loss in BACHD mouse model for Huntington's disease. *Eur J Neurosci* 45:785–796. <https://doi.org/10.1111/ejn.13510>.